A Momentum Budget Analysis of Westerly Wind Events Associated with the Madden–Julian Oscillation during DYNAMO

JI-HYUN OH, XIANAN JIANG, AND DUANE E. WALISER

Joint Institute for Regional Earth System Science and Engineering, University of California, Los Angeles, Los Angeles, and Jet Propulsion Laboratory, California Institute of Technology, Pasadena, California

MITCHELL W. MONCRIEFF

National Center for Atmospheric Research, Boulder, Colorado*

RICHARD H. JOHNSON AND PAUL CIESIELSKI

Colorado State University, Fort Collins, Colorado

(Manuscript received 10 February 2015, in final form 14 June 2015)

ABSTRACT

The Dynamics of the Madden–Julian Oscillation (DYNAMO) field campaign was conducted over the Indian Ocean (IO) from October 2011 to February 2012 to investigate the initiation of the Madden–Julian oscillation (MJO). Three MJOs accompanying westerly wind events (WWEs) occurred in late October, late November, and late December 2011. Momentum budget analysis is conducted to understand the contributions of the dynamical processes involved in the wind evolution associated with the MJO over the IO during DYNAMO using European Centre for Medium-Range Weather Forecasts analysis. This analysis shows that westerly acceleration at lower levels associated with the MJO active phase generally appears to be maintained by the pressure gradient force (PGF), which could be partly canceled by meridional advection of the zonal wind. Westerly acceleration in the midtroposphere tends to be mostly attributable to vertical advection. The results herein imply that there is no simple linear dynamic model that can capture the WWEs associated with the MJO and that nonlinear processes have to be considered.

In addition, the MJO in November (MJO2), accompanied by two WWEs (WWE1 and WWE2) spaced a few days apart, is diagnosed. Unlike other WWEs during DYNAMO, horizontal advection is more responsible for the westerly acceleration in the lower troposphere for WWE2 than the PGF. Interactions between the MJO2 envelope and convectively coupled waves (CCWs) are analyzed to illuminate the dynamical contribution of these synoptic-scale equatorial waves to the WWEs. The authors suggest that different developing processes among WWEs can be attributed to different types of CCWs.

1. Introduction

The discovery of the Madden–Julian oscillation (MJO) in the early 1970s has led to diverse and intensive research on the MJO in terms of its evolution, structure, and impact on other atmospheric phenomena [Madden and Julian 1971, 1972; see review by Zhang (2005); Lau and Waliser 2012]. The global-scale MJO, consisting of a hierarchy of multiscale convective systems, develops over the Indian Ocean (IO) and propagates eastward along the equator at a phase speed of about $5\,\mathrm{m\,s^{-1}}$ (Nakazawa 1988; Takayabu 1994; Roundy 2008; Kiladis et al. 2009).

The zonal circulation of the MJO is characterized by low-level westerlies (easterlies) in and to the west (east) of the convective center (Knutson and Weickmann 1987; Zhang 2005; Seiki and Takayabu 2007). The direction of zonal winds in the upper troposphere is

* The National Center for Atmospheric Research is sponsored by the National Science Foundation.

Corresponding author address: Dr. Ji-Hyun Oh, Jet Propulsion Laboratory, California Institute of Technology, MS 233-300, 4800 Oak Grove Drive, Pasadena, CA 91109.
E-mail: ji-hyun.oh@jpl.nasa.gov

DOI: 10.1175/JAS-D-15-0044.1

opposite to that in the lower troposphere. In addition to the convective signal as an identifier of the MJO initiation (Matthews 2008), certain characteristics of the zonal circulation have been used as a standard metric for monitoring the state of MJO and investigating features of the MJO (Wheeler and Hendon 2004; Jiang et al. 2011; Barnes and Houze 2013; Yoneyama et al. 2013; Zhang et al. 2013; Straub 2013). It is also accepted that the low-level MJO winds play a role by inducing surface turbulent fluxes that support the MJO convection (Maloney and Sobel 2004; Araligidad and Maloney 2008; Sobel et al. 2008, 2010). In addition, it has been noted that the westerly wind events (WWEs) associated with the MJO can impact El Niño–Southern Oscillation (ENSO) (Zhang 2005; Hendon et al. 2007; Seiki and Takayabu 2007).

Despite considerable effort made toward improving the prediction skill of the MJO, critical challenges still remain for current general circulation models (GCMs) to more accurately represent the MJO and, in particular, its initiation over the IO. Dominated by seasonally changing monsoon flow, the IO is a unique setting particularly for the MJO whose features strongly depend on the seasonal cycle (Rui and Wang 1990).

Despite the frequent occurrence of WWEs over the IO [Fig. 3 of Seiki and Takayabu (2007)] and different spatial relationships between convection and wind associated with the MJO (Kerns and Chen 2014), previous studies have focused largely on the WWEs over the western Pacific where the eastward-propagating MJO convection redevelops after its weakening over the Maritime Continent (Kessler et al. 1995; Carr and Bretherton 2001; Lin et al. 2005; McPhaden et al. 2006; Seiki et al. 2011). In particular, the Tropical Ocean and Global Atmosphere Coupled Ocean–Atmosphere Response Experiment (TOGA COARE), with two major MJOs during the intensive observing period from 1 November 1992 through 28 February 1993, has provided opportunities for detailed studies on the WWEs that occurred over the western Pacific warm pool (Lin and Johnson 1996; Yanai et al. 2000; Carr and Bretherton 2001; Tung and Yanai 2002a,b; Lin et al. 2005).

Using Doppler radar data, Houze et al. (2000) identified strong midlevel inflow in the stratiform regions of mesoscale convective systems (MCSs) during the westerly onset and in regions of strong westerly winds associated with the Kelvin–Rossby wave pattern. They postulated that the mesoscale inflow transports easterly momentum downward, reducing the westerlies near the surface in the westerly onset region, while in the strong westerly region, the mesoscale inflow jet brings westerly momentum downward, enhancing the surface westerlies. Numerical simulations by Lafore and Moncrieff (1989) showed that the strong midtropospheric inflow at the rear of mesoscale convective systems is driven by the horizontal pressure gradient arising from potential temperature gradients that are generated by latent heating in the convective region and unsaturated evaporation-driven mesoscale descent.

On the basis of residual momentum budget analysis, and utilizing objectively analyzed soundings during TOGA COARE, Tung and Yanai (2002a,b) demonstrated the transfer of kinetic energy from convection to large-scale westerly wind events. They concluded that the upscale energy transfer is promoted at the onset of the MJO low-level westerlies, while convective momentum transport (CMT) largely acted as a frictional damping in the mature stage that has strong low- to middle-level westerlies, by decelerating the large-scale zonal flow. Adopting the findings by Tung and Yanai (2002a,b) to their theoretical model experiments, Khouider et al. (2012) highlighted two-way interactions between convectively coupled waves (CCWs) and the background MJO winds through the CMT.

In addition, Lin et al. (2005) examined a zonal momentum budget associated with the MJO over the equatorial western Pacific using 15 years of daily global reanalysis data. According to their study, the pressure gradient force (PGF) plays a major role in driving MJO zonal winds throughout entire troposphere. This strong forcing is balanced by the vertical advection of perturbation zonal wind by the mean vertical motion and zonal advection of the mean zonal wind by the perturbation zonal wind in the upper troposphere. In addition, the meridional advection of the zonal wind by the perturbation meridional wind and the budget residual, representing all subgrid-scale processes, act primarily as a damping effect to balance the PGF in the lower troposphere.

The Dynamics of the Madden–Julian Oscillation (DYNAMO) field campaign was conducted over the IO from October 2011 to February 2012 to investigate the initiation of the MJO over the IO and improve our forecasting skill of the MJO (Yoneyama et al. 2013). This international effort yielded unprecedented high-quality datasets including observations from ground-based radars, upper-air soundings, aircraft, ships, and satellites to benefit comprehensive studies of the mechanisms related to the initiation of the MJO over the IO (Johnson and Ciesielski 2013; Yoneyama et al. 2013).

Three MJOs, each accompanied by one or more WWEs, occurred in late October, late November, and late December 2011 (Gottschalck et al. 2013; Moum et al. 2014; Yoneyama et al. 2013). We refer to these three events as MJO1, MJO2, and MJO3, respectively. A more detailed description and large-scale context of

these MJOs can be found in, for example, Yoneyama et al. (2013), Gottschalck et al. (2013), and Johnson and Ciesielski (2013). In particular, MJO2 is intriguing for its diverse characteristics. Two bursts of westerly winds along with two rainfall peaks were observed in association with MJO2 (Moum et al. 2014). Furthermore, the excellent availability of data collected by all instruments in the field made MJO2 an ideal case for detailed studies (Fu et al. 2013; Judt and Chen 2014; Kerns and Chen 2014).

The purpose of our study is to investigate the generation of low-level westerly winds during the MJO life cycle. The synoptic-scale WWEs were also embedded in the low-level westerly wind component of the MJO (Zhang 2005; Chiodi et al. 2014). Zhang (2005) pointed out the confusion among the concepts for the westerly winds at different time scales. For brevity, the term WWE, as used in this study, refers to all significant low-level westerly wind signals lasting from a few days to 2 weeks coincident with the MJO events during DYNAMO. We perform the momentum budget analysis to understand the respective contributions of various processes involved in the wind evolution associated with the MJO over the IO during DYNAMO using European Centre for Medium-Range Weather Forecasts (ECMWF) operational analyses. This study focuses on the zonal momentum budget, since the circulation during MJO life cycle is more noticeable in zonal than meridional winds (Madden and Julian 1971).

In addition to the analysis of the momentum budget to shed light on common features of the MJO events in 2011 DYNAMO, the unusual behavior of MJO2 is investigated in detail. Previous studies highlighted the interaction between the MJO convective envelope and CCWs during DYNAMO field campaign (Moum et al. 2014; DePasquale et al. 2014; Kerns and Chen 2014). Using TRMM precipitation, Gottschalck et al. (2013) and Moum et al. (2014) identified two convectively coupled Kelvin waves moving rapidly eastward within an envelope of MJO2 and documented that these Kelvin waves contributed to the heavy precipitation amounts observed during MJO2. Meanwhile, Kerns and Chen (2014) emphasized westward-moving Rossby wave–like systems, presumably consisting of an equatorial Rossby (ER) wave or mixed Rossby–gravity (MRG) waves within the eastward-propagating MJO2 envelope. They noted that the Rossby wave–like systems were responsible for the second rainfall peak as well as a dry-air intrusion during the MJO2 (Sobel et al. 2014; Wang et al. 2015). In light of previous studies, the dynamical contribution of these synoptic-scale equatorial waves to the WWEs during MJO2 will be examined.

This study is structured as follows. Datasets and methods used for the analysis are discussed in section 2. In section 3, kinematic features of the MJOs are described. In section 4, common features of WWE generation in the momentum budget associated with the MJO events are examined. Section 5 contains a further detailed investigation of WWEs during MJO2. A summary and conclusions are presented in section 6.

2. Data and methods

a. Data

The ECMWF operational analyses on pressure levels are used to compute momentum budget terms. The dataset, generated by Cy37r2 and Cy37r3 versions of the Integrated Forecast System (IFS) truncated at wavenumber T1279 (~16 km), was archived with a 0.25° spatial resolution, 25 vertical levels from the surface to 1 hPa, and a 6-hourly interval. Effects of cloud-scale horizontal pressure gradient are accounted for with a treatment of the vertical transport of horizontal momentum by convection in this model (Gregory 1997).[1] More details can be found in Ling et al. (2014). The data from DYNAMO field observations were assimilated to produce the ECMWF analyses (Johnson and Ciesielski 2013).

For comparison to the model analysis, the Colorado State University (CSU)–DYNAMO upper-air and surface gridded analyses, version 3a (CSU v3a), based entirely on observations (i.e., no model input), which includes soundings, satellite winds, and Constellation Observing System for Meteorology, Ionosphere, and Climate (COSMIC) profiles, are used. The dataset has 1° spatial resolution and 25-hPa vertical resolution between 1000 and 50 hPa at a 3-hourly interval. The DYNAMO enhanced sounding network consists of two quadrilateral arrays covering the longitude band from about 73° to 80°E over the Indian Ocean. The Northern Sounding Array (NSA) covers from the equator to 5°N, whereas the Southern Sounding Array (SSA) covers from 7°S to the equator. Further detailed documentation of datasets can be found in Johnson and Ciesielski (2013), Ciesielski et al. (2014), and Johnson et al. (2015).

Additionally, 3-hourly Tropical Rainfall Measuring Mission (TRMM) 3B42 (version 7; Huffman et al. 1995) rainfall data are utilized to identify the convection related to the MJO. High-quality passive and active microwave estimates calibrated with infrared (IR) estimates are combined with rain gauge analyses to generate the TRMM data. The spatial coverage of this

[1] http://old.ecmwf.int/research/ifsdocs/CY37r2/IFSPart4.pdf.

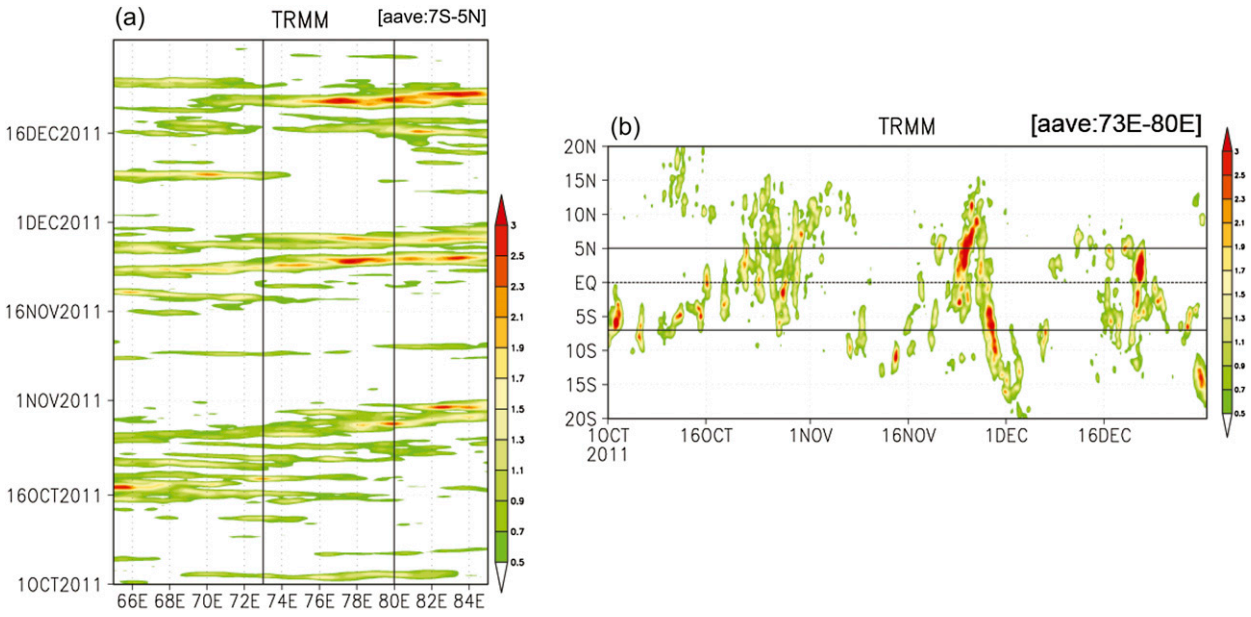

FIG. 1. (a) Time–longitude diagram of TRMM rain rate (mm h^{-1}) averaged between 7°S and 5°N and (b) latitude–time diagram of TRMM rain rate averaged between 73° and 80°E for the DYNAMO 2011 period. Solid black lines indicate the boundaries of DYNAMO enhanced sounding arrays.

dataset is from 50°S to 50°N over the globe with a 0.25° longitude–latitude resolution.

b. Methods

The budget of the zonal momentum is computed as

$$\frac{\partial u}{\partial t} = -u\frac{\partial u}{\partial x} - v\frac{\partial u}{\partial y} - \omega\frac{\partial u}{\partial p} - \frac{\partial \varphi}{\partial x} + fv + X, \qquad (1)$$

where u is the zonal wind, v is the meridional wind, ω is the vertical pressure velocity, φ is the geopotential, f is the Coriolis parameter, and X is the time rate of change of the zonal wind due to unresolvable processes. Each budget term is calculated at each grid point using 6-hourly ECMWF analysis data. The zonal and meridional advection terms are computed using spherical harmonics, and the vertical advection term is calculated using centered finite differences. Although the ECMWF analysis data used in this study have relatively high spatial resolution (0.25°) for a global dataset and take advantage of the intensive observations during DYNAMO, it is impossible to obtain a completely closed budget of momentum as a result of all effects from subgrid-scale processes including the acceleration through the convergence of momentum flux due to convection and other turbulence, errors in the computation and the data, and analysis increment. Therefore, we focus primarily on dominant terms of the momentum budget at grid scale of the analysis, rather than examine all budget terms and their closure in detail.

3. Overall features and comparison to observation during 2011 DYNAMO

Figure 1a shows longitude–time sections of TRMM 3B42 precipitation data averaged over the latitudinal band 7°S–5°N during the DYNAMO 2011 observation period. Vertical black lines denote longitudinal boundaries of the NSA and SSA (73° and 80°E, respectively). Three MJO events were noted during this period: for example, two prominent events in late October and late November and one ''mini MJO'' (Gottschalck et al. 2013) in late December 2011. Figure 1b is a latitude–time diagram of TRMM 3B42 precipitation averaged over longitudes of the sounding arrays (73°–80°E). Horizontal black solid lines indicate latitudinal boundaries of NSA and SSA. The regions of vigorous convection associated with the MJO events shift southward with time, resulting in more precipitating area over the NSA during the early part of DYNAMO and over the SSA during the latter part of 2011 observing period (Johnson and Ciesielski 2013; Yoneyama et al. 2013). With this in mind, our analysis is mainly focused on the NSA from October to December in 2011, in which the CSU v3a datasets are available and more convective related activities can be distinctly identified.

Figure 2 illustrates features of vertical structure associated with the three MJO events throughout DYNAMO 2011 by comparing the time series of 5-day running-mean vertical profiles of pressure velocity (Figs. 2a,b), apparent heating source Q_1(Figs. 2c,d), and

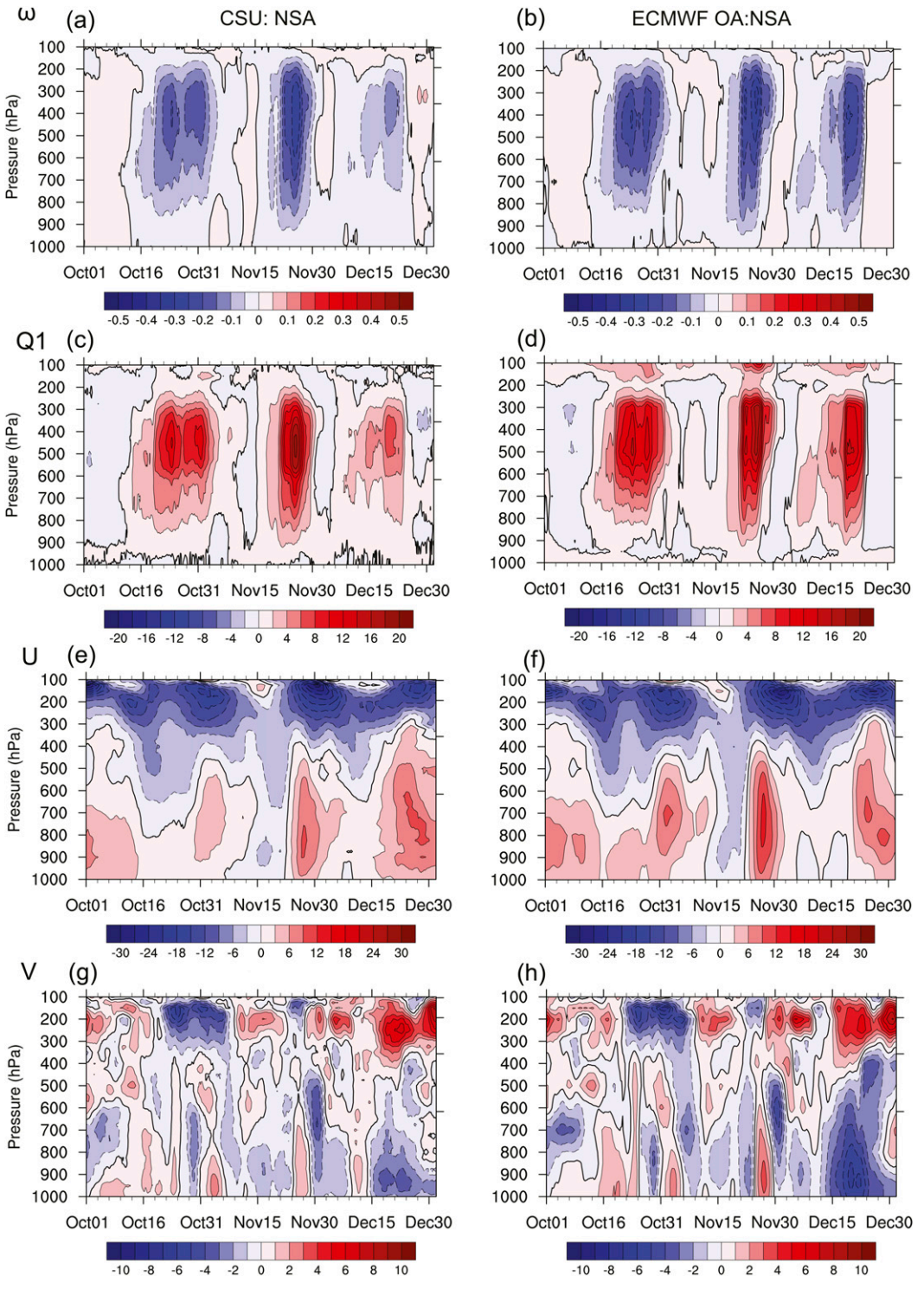

FIG. 2. Time–pressure sections of NSA-averaged (0°–5°N, 73°–80°E) (a),(b) pressure velocity (Pa s^{-1}), (c),(d) apparent heating source (K day^{-1}), (e),(f) zonal wind (m s^{-1}), and (g),(h) meridional wind (m s^{-1}) for (left) CSU, version 3a and (right) ECMWF analysis data. A 5-day running mean is applied to all variables.

zonal (Figs. 2e,f) and meridional wind (Figs. 2g,h) obtained from the CSU v3a datasets (left column) and the ECMWF analysis (right column) averaged over the NSA. Note that for the sake of calculation convenience, a rectangular region is chosen for the NSA (0°–5°N, 73°–80°E) in this study, which is slightly different from the actual spatial coverage of the sounding arrays shown in Fig. 1 of Johnson and Ciesielski (2013). Overall, the ECMWF analyses agree well with the CSU v3a fields except for Q_1 above 150 hPa and after 15 December when the northern sounding sites of the NSA ended operations. The generally good consistency lends confidence that the ECMWF analyses have a credible quality to conduct the momentum budget analysis. Figures 2a and 2b illustrate deep ascending motions with peaks between 500 and 250 hPa in late October, late November, and late December, respectively, closely related to the passage of the active MJO phases over the NSA.

The evolution of Q_1 throughout DYNAMO 2011 from CSU v3a data and ECMWF analyses are illustrated in Figs. 2c and 2d, respectively. The discrepancies in Q_1 above 150 hPa between CSU v3a data and ECMWF analyses are possibly related to cloud and temperature biases in ECMWF analyses. Nonetheless, the maxima in Q_1 correspond to the period of strong upward motion. Johnson et al. (2015) provided a detailed description of two maxima in Q_1 associated with MJO1 and MJO2, pointing out the stepwise evolution of cloud morphology within the MJO—namely, shallow nonprecipitating cumulus, followed by congestus, then deep convection, and finally stratiform clouds. The strong upward motion along with increases in the amplitude of Q_1 was followed by WWEs with their maxima at about 700 hPa and easterlies in the upper troposphere (Figs. 2e,f). Interestingly, the westerlies during the late-December MJO expanded higher (up to near 200 hPa) than those in the first and second MJO events. It has been argued whether the third event can legitimately be identified as an "MJO" (Gottschalck et al. 2013; Yoneyama et al. 2013; Kiladis et al. 2014). Contrary to the MJOs in late October and late November, the MJO in December is not categorized as an MJO when applying a standard MJO tracking method based on the real-time multivariate MJO (RMM) index (Gottschalck et al. 2013; Yoneyama et al. 2013; Kiladis et al. 2014). Nevertheless, the eastward-propagating signal associated with the late-December event was detected by 30–96-day eastward-only filtered OLR (Kiladis et al. 2014); therefore, the late-December event is generally referred to as an MJO (Gottschalck et al. 2013; Yoneyama et al. 2013).

While strong upward motion and the baroclinic structure of the zonal wind are common features associated with the active MJO phases in Fig. 2, the behavior of low-level meridional wind varies among these the MJO events (Figs. 2g,h). Furthermore, the magnitude of the meridional wind is weaker than that of the zonal wind. While the direction of low-level meridional wind varied for the late-October and late-November MJO events, northerly winds persisted for the MJO in late December. The southward shift of convection with time is responsible for this difference (Fig. 1b).

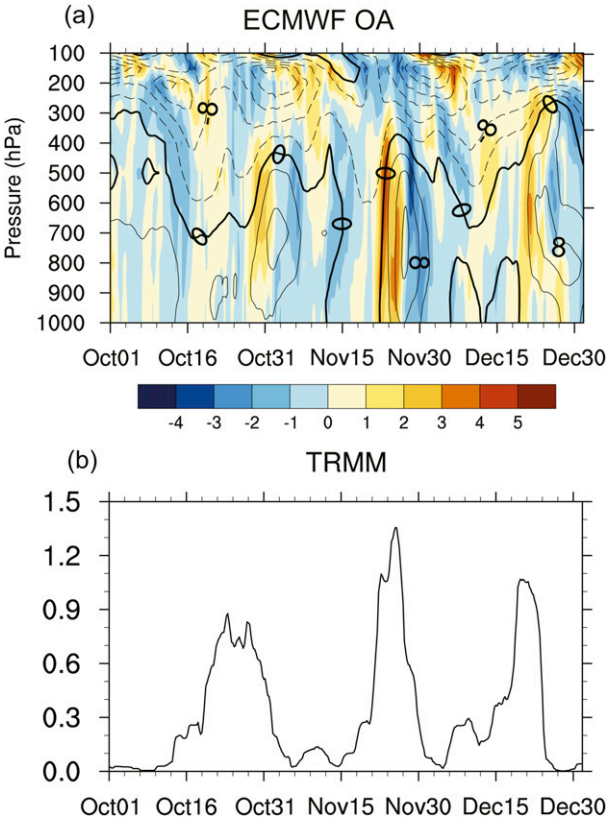

FIG. 3. (a) Time–pressure sections of the NSA-averaged (0°–5°N, 73°–80°E) zonal wind (m s^{-1}; contours) and zonal-wind tendency (m s^{-1} day^{-1}; shading with 1 m s^{-1} day^{-1} interval) of ECMWF operational analysis. Zero line has been thickened. Solid contours denote positive values, while dashed contours denote negative values. (b) Time series of TRMM rain rate (mm h^{-1}) averaged over the NSA. A 5-day running mean has been applied to all variables.

Figure 3a shows the 5-day running-mean time series of zonal wind (contoured) and its tendency (shading) from the ECMWF analysis averaged over the NSA. The 5-day running mean of TRMM 3B42 precipitation is displayed in Fig. 3b. Clearly evident is the strong convective activity associated with the MJO and the coincident westerly (easterly) acceleration at lower (upper) levels, resulting in the predominant baroclinic wind structure. Particularly noteworthy is the maximum westerly acceleration aloft over a deep layer centered near 600 hPa.

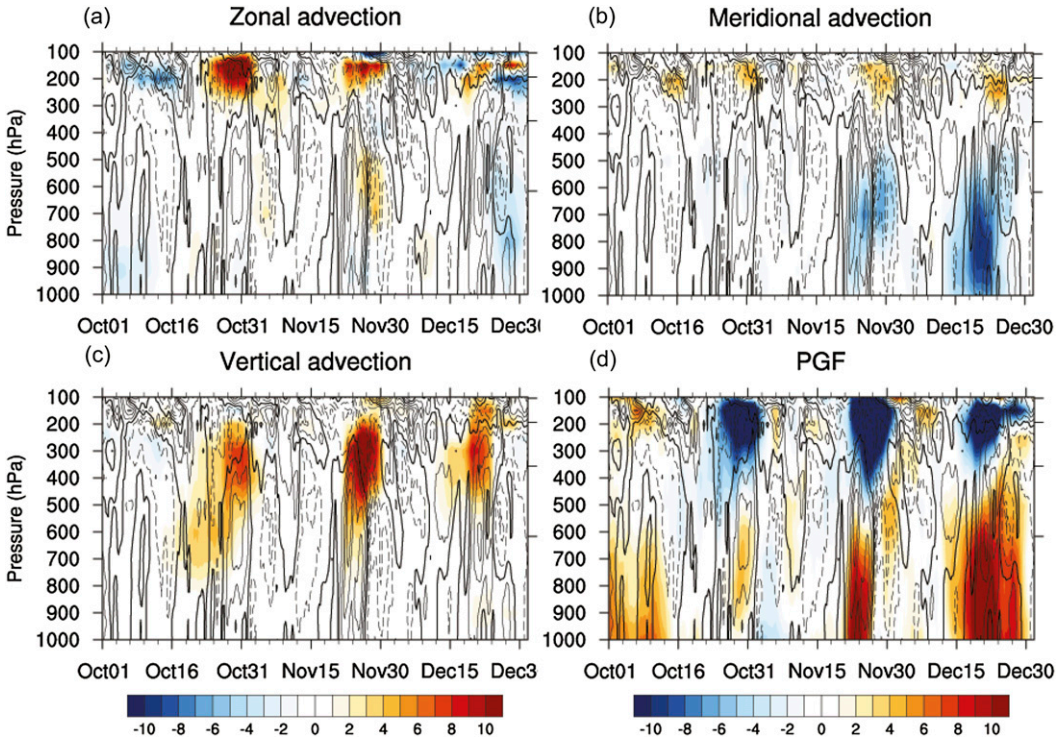

FIG. 4. Time–pressure diagram of terms of momentum budget ($m\,s^{-1}\,day^{-1}$; shaded): (a) zonal advection, (b) meridional advection, (c) vertical advection, and (d) pressure gradient force of ECMWF analysis data averaged over NSA array (0°–5°N, 73°–80°E). Zonal-wind tendency is overlaid (contours; dashed for negative values; solid for positive values) in each panel. A 5-day running mean is applied to all terms.

4. Zonal momentum budget during DYNAMO

We examine the relative contribution of the various terms in Eq. (1) to the zonal-wind tendency averaged over the NSA using ECMWF analyses to assess which terms play a dominant role in determining the baroclinic structure of zonal winds as seen in Figs. 2f and 3a. Figure 4 shows time–pressure plots of the 5-day running-mean zonal advection (Fig. 4a), meridional advection (Fig. 4b), vertical advection (Fig. 4c), and PGF (Fig. 4d), respectively. The Coriolis force is not shown because of its smaller magnitude near the equator compared to the other terms in Eq. (1). Contours overlaid in each panel denote the local tendency of the zonal wind. Consistent with Trier et al. (1998), the local tendency of the zonal wind is weaker than the individual forcing terms because of substantial cancellation among the forcing components. As a check on the accuracy of the estimation of the advection and PGF terms, the tendency predicted from a sum of the forcing terms on the right-hand side of Eq. (1) is compared to the actual tendency calculated from the wind components (not shown). The resulting correspondence between the sum of forcing terms and the actual tendency gives us confidence to conduct further analysis despite the existence of a significant residual above 200 hPa. However, the magnitude of the residual term below 200 hPa is relatively small.

The PGF in the lower and upper troposphere is the most dominant forcing term in the momentum budget for the local tendency of zonal wind related to the MJO active phase, and it has a dipole structure with a positive sign below 500 hPa and a negative sign above 500 hPa during each MJO active phase (Fig. 4d). The vertical structure of PGF is in phase with that of the zonal-wind tendency, especially at every passage of the MJO active phase. In contrast, the meridional advection term tends to have a vertical structure that is opposite to the two-layer PGF structure (Fig. 4b). In the lower troposphere (below 500 hPa), the meridional advection term partially balances the PGF, reducing the total westerly acceleration associated with the MJO active phase. Analogously, the zonal advection term partially offsets the PGF (Fig. 4a) in the upper troposphere (above 300 hPa), decreasing the net easterly acceleration related to the MJO active phase.

It is of particular interest to note that the vertical advection term is dominant at inducing westerly acceleration mostly between 700 and 200 hPa during the MJO active phases with strong vertical shear of zonal wind and upward motion. Furthermore, the vertical advection

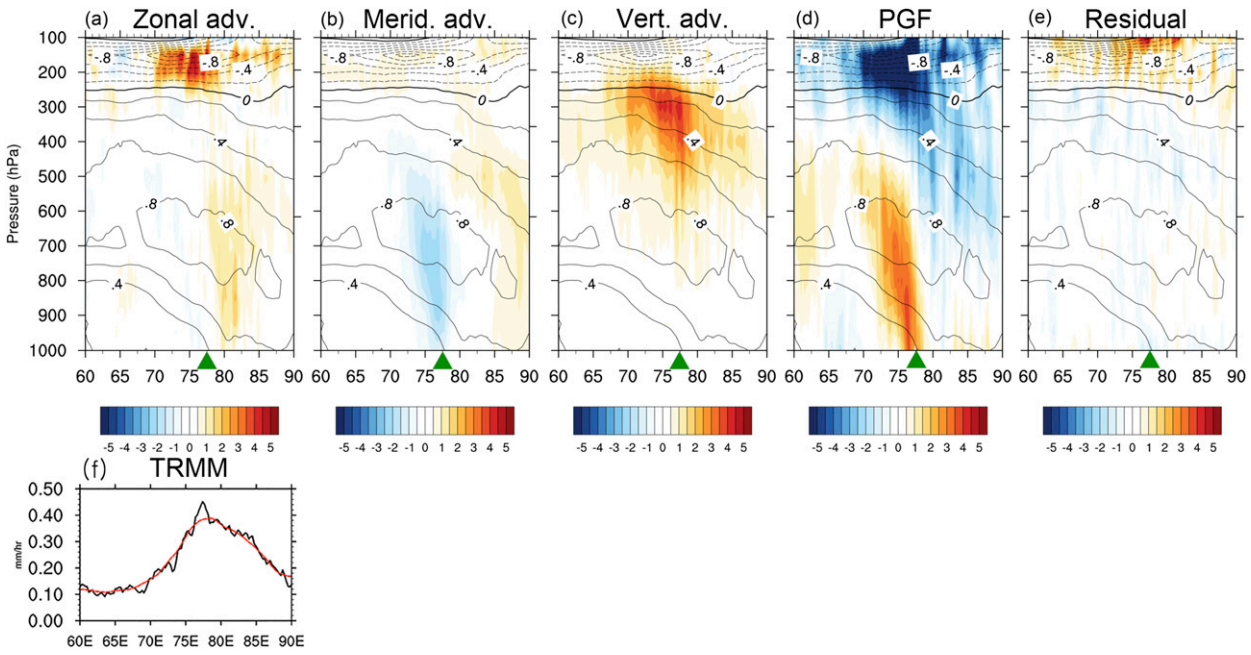

FIG. 5. Longitude–pressure diagrams of regressed forcing terms against TRMM 3B42 precipitation averaged over northern array for DYNAMO observing period in 2011: (a) zonal advection, (b) meridional advection, (c) vertical advection, (d) pressure gradient force, and (e) residual. Contours denote regressed local tendency of zonal wind ($m\,s^{-1}\,day^{-1}$). (f) Regressed TRMM rain onto NSA-averaged TRMM rain (black) along with 5-day running mean of regressed TRMM rain (red). All regressed variables are averaged between 0° and 5°N. Green triangle in (a)–(e) indicates the longitudinal location of the rainfall peak.

term related to the MJO1 and MJO2 tends to gradually rise in the vertical with time, indicating the upward transport of momentum by updrafts. At lower levels, the vertical advection tends to be in phase with the local tendency that is inducing westerlies. On the other hand, at levels above around 250 hPa, this term is out of phase with the local tendency, decelerating the easterlies.

To quantify the role of the individual terms in the zonal momentum budget in modulating the circulation associated with the MJO, we regress the individual forcing terms shown in Fig. 4, as well as the budget residual, at all grid points within the NSA onto TRMM 3B42 precipitation averaged over the NSA. Although special caution is required when interpreting the budget residual owing to contamination by errors in the other terms of Eq. (1) and unknown analysis increment, the residual in the free troposphere is considered to largely account for the effect of CMT (Carr and Bretherton 2001; Tung and Yanai 2002a,b; Lin et al. 2005).

Figure 5 displays the longitude–pressure diagram of the regressed terms in the u-momentum budget (Figs. 5a–d) along with the residual (Fig. 5e) averaged between the equator and 5°N. The regressed local tendency of the u wind is overlaid in each panel with contours. The in-phase (out of phase) relationships between the local tendency and terms on the right-hand side of Eq. (1) imply the term acts as a driving (damping) factor. In addition, Fig. 5f illustrates the regressed TRMM 3B42 precipitation onto the NSA-averaged rainfall, indicating the longitudinal location of the convective center. Additionally, Fig. 6a displays a profile of the regressed local tendency of zonal wind averaged over the NSA, and Fig. 6b shows profiles of regressed forcing terms corresponding to the regressed local tendency. The regressed local tendency indicates westerly acceleration from the surface to 250 hPa with a peak near 700 hPa and easterly acceleration above 250 hPa (contours in Fig. 5a–e and profile in Fig. 6a).

While the PGF term is the dominant contributor to the westerly acceleration from the surface to 600 hPa (Fig. 5d and black line in Fig. 6b), the meridional advection counteracts the PGF in the lower troposphere (Fig. 5b and green line in Fig. 6b), interfering with the establishment of low-level westerlies. On the other hand, vertical advection transporting westerly momentum upward is the largest contributor to the total westerly acceleration at levels higher than 600 hPa, resulting in a positive net acceleration between 600 and 250 hPa (Fig. 5c and purple line in Fig. 6b). The vertical advection, closely associated with convection but also impacting the momentum tendency equation (Mapes et al. 2006), shows a westward tilted vertical structure in Fig. 5c.

The CMT defined by the residual in Tung and Yanai (2002b) is known to play a potential role in the westerly

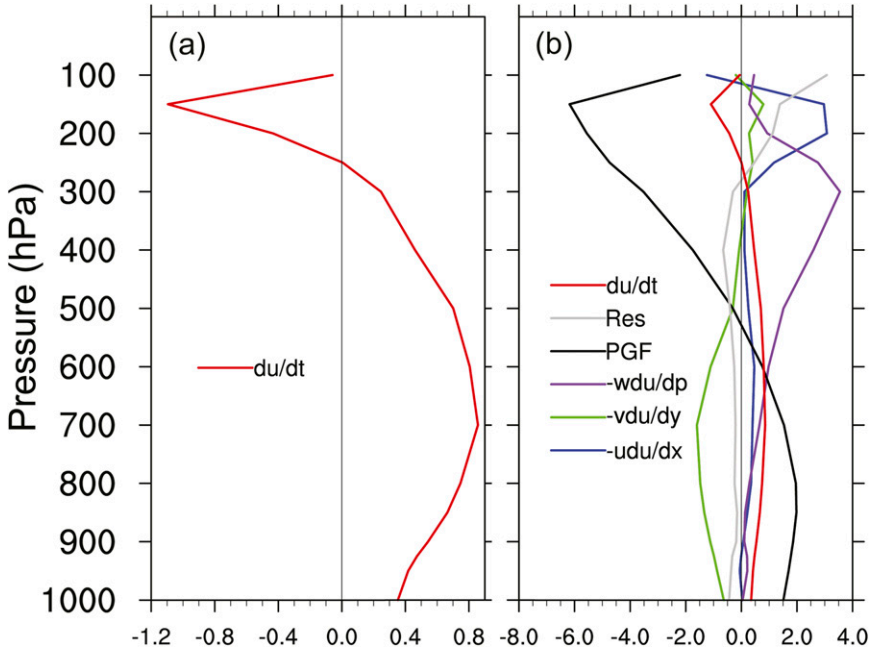

FIG. 6. Profiles of regressed (a) zonal-wind tendency and (b) terms of the zonal momentum budget onto TRMM rain rate averaged over northern array (0°–5°N, 73°–80°E) from 1 Oct to 31 Dec 2011 ($m\,s^{-1}\,day^{-1}$). Regressed variables are averaged over the NSA.

acceleration either in the westerly onset regime or in the strong westerly regime (Houze et al. 2000). In our analysis, however, the residual that includes all the subgrid processes as well as analysis increment acts to damp the preexisting easterly flow in the upper troposphere above 200 hPa in the vicinity of the convective center (75°E) (Fig. 5e and gray line in Fig. 6b). The noticeable damping in the upper troposphere may result from detrainment at the cloud top (Yang and Houze 1996). Nevertheless, the residual and the zonal advection terms in the lower troposphere are negligible compared to other terms in Eq. (1) (Fig. 6b).

Our result is consistent with the findings of Lin et al. (2005) based on 15 years of global reanalysis data and Miyakawa et al. (2012) based on a global cloud-resolving model. Although Lin et al. (2005) primarily focused on the zonal momentum budget based on the 30–70-day filtered departures from the zonal mean, which differs from our approach based on total zonal momentum budget, they also found that the advection due to zonal and vertical components contributes to the MJO zonal momentum budget in the upper troposphere while the meridional component results in zonal wind damping in the lower troposphere. On the other hand, defining large-scale terms as the horizontal-mean values within a 5°-radius rain area associated with a MJO event to represent resolvable-scale circulations in a GCM, Miyakawa et al. (2012) presented the dominant contributions of PGF, vertical advection, and meridional advection to the MJO zonal-wind acceleration consistent with our result. However, their emphasis was rather on the zonal acceleration due to vertical momentum flux convergence associated with winds departing from the horizontal mean, which they called the zonal acceleration due to CMT.

We now consider the mechanisms by which three major terms—the PGF, vertical advection, and meridional advection—modify the atmospheric circulation associated with the MJOs throughout 2011 DYNAMO. Figure 7a shows a longitude–pressure diagram of the regressed geopotential height (contours) and Q_1 (shading) onto the TRMM 3B42 precipitation averaged over the NSA. The maximum heating between 500 and 300 hPa from 75° to 80°E is collocated with the peak of the regressed rainfall as shown in Fig. 5f, indicating the release of latent heat by condensation over the region of strong convection. In the vicinity of this region, there exists a noticeable longitudinal gradient of the geopotential height at lower levels (decreasing from west to east) and a reversed gradient at upper levels, driving westerly (easterly) acceleration in the lower (upper) troposphere.

Along with the geopotential height decreasing (increasing) from west to east at 850 (200) hPa (shading) in the vicinity of the rainfall region over the NSA (contours), the horizontal circulation driven by the release of

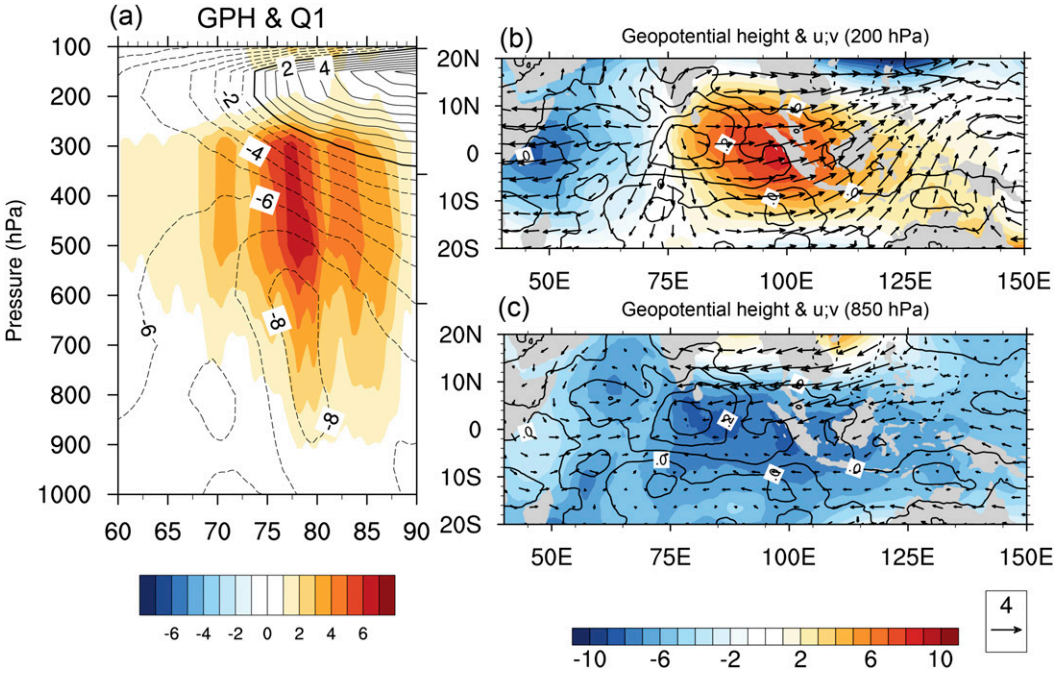

FIG. 7. (a) Longitude–pressure diagram of regressed Q_1 (K day^{-1}; shading) and geopotential height (GPH; m; contours) onto TRMM 3B42 precipitation averaged over northern array for DYNAMO observing period in 2011. The regressed variables are averaged between 0° and 5°N. (b),(c) Longitude–latitude plots of the regressed TRMM 3B42 rainfall (mm h^{-1}; contours), geopotential height (m; shading), and horizontal wind (m s^{-1}; vectors) onto TRMM 3B42 precipitation averaged over northern array for DYNAMO observing period in 2011 at 200 hPa in (b) and 850 hPa in (c).

latent heat due to the rainfall over the NSA is conspicuous (vectors) in Figs. 7c and 7b. In addition to the zonal gradient of the geopotential height in the vicinity of rainfall peak, the two cyclonic circulations associated with the Rossby gyres could be possible contributors to the WWE resulting in a zone of westerlies between the two gyres as suggested by Takayabu et al. (1999). Meanwhile, distinct divergent outflow at 200 hPa is also shown in the enhanced convective region, resulting in anomalous easterlies (westerlies) to the west (east) of the convection.

We have shown that vertical advection can play a significant role in the zonal momentum budget. Moreover, it is noteworthy that the MJO, a planetary-scale disturbance with zonal wavenumbers 1–3, is recognized as an organization of a hierarchy of multiscale convective systems (Nakazawa 1988; Moncrieff et al. 2012). Therefore, in order to better understand any MJO event, the convective systems at different scales embedded in the MJO should be taken into account. For example, Zuluaga and Houze (2013) identified 11 rain episodes with 2–4-day periods in active phases of MJO1–3 by using ground-based radar data during DYNAMO. To further understand the role of vertical advection, we decompose the zonal-wind and pressure velocity fields of the vertical advection term into low-frequency (5-day running mean: $\overline{u}$ and $\overline{\omega}$) and high-frequency (deviation from 5-day running mean: u' and ω') components.[2] The partitioning yields four terms as follows:

$$-(\overline{\omega}+\omega')\frac{\partial(\overline{u}+u')}{\partial p} = -\overline{\omega}\frac{\partial\overline{u}}{\partial p} - \overline{\omega}\frac{\partial u'}{\partial p} - \omega'\frac{\partial\overline{u}}{\partial p} - \omega'\frac{\partial u'}{\partial p}. \quad (2)$$

Figure 8 shows time–pressure plots for each term on the right-hand side of Eq. (2) averaged over the NSA during DYNAMO in 2011. Among the four terms in Eq. (2), the low-frequency component ($-\overline{\omega}\partial\overline{u}/\partial p$; Fig. 8a) and high-frequency component ($-\omega'\partial u'/\partial p$; Fig. 8d) of vertical advection are predominant. The vertical pattern of the low-frequency component resembles that of the total vertical advection shown in Fig. 4c, except that the low-frequency component is considerably smoother than the total vertical advection. This indicates that the total vertical zonal momentum transport during the MJO active phases was dominated by the low-frequency

[2] Sensitivity tests were conducted by decreasing the period of running mean to 2 days, but the results did not change significantly.

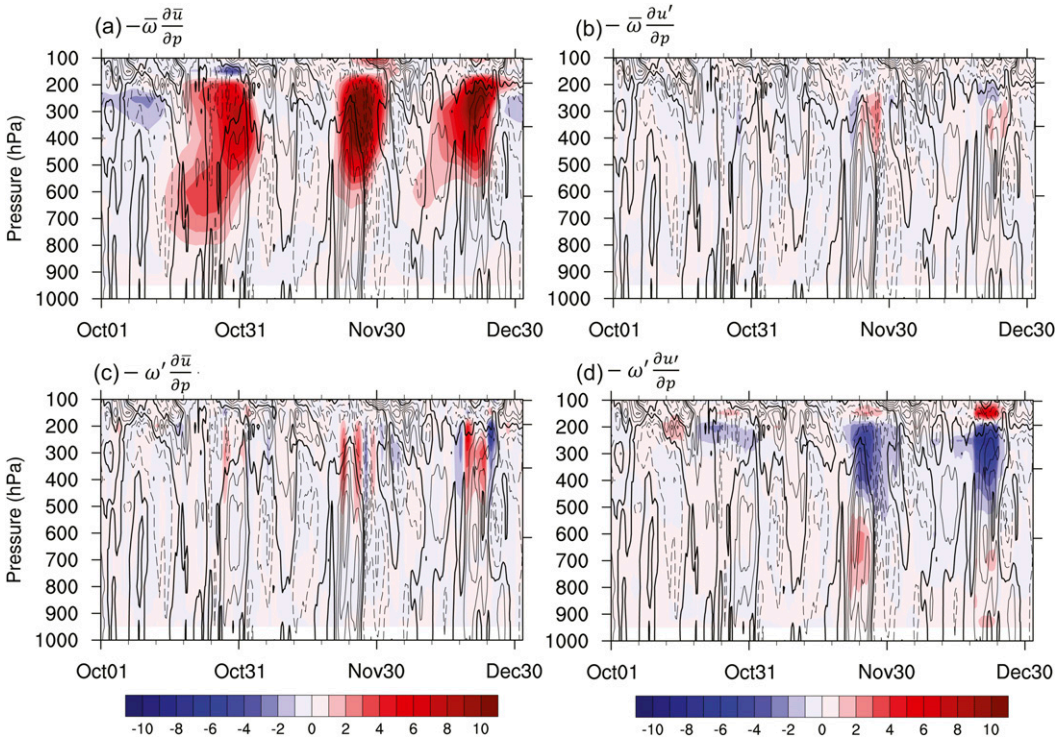

FIG. 8. Time–pressure diagram of decomposed vertical advection ($\mathrm{m\,s^{-1}\,day^{-1}}$) (a) $-\overline{\omega}\partial\overline{u}/\partial p$, (b) $-\overline{\omega}\partial u'/\partial p$, (c) $-\omega'\partial\overline{u}/\partial p$, and (d) $-\omega'\partial u'/\partial p$. Zonal-wind tendency is overlaid (contour; dashed for negative values; solid for positive values) in each panel. A 5-day running mean is applied to all terms.

transport in which the environmental flow or equatorial waves (i.e., Kelvin or Rossby waves) with periods longer than a 5-day time scale could be involved (Kiladis et al. 2009). On the other hand, it is noteworthy that the vertical structure of the high-frequency vertical advection has a three-layer structure with a positive sign in the upper and lower troposphere and a negative sign in the midtroposphere, coincident for MJO active phases. The sign of high-frequency component is opposite to the mean flow, which suggests a countergradient transport. However, it is a small contribution and offset by large-scale vertical transport of zonal momentum, which seems to be predominately downgradient (Fig. 8a). Shorter than the 5-day time scale, equatorial synoptic waves, such as 2-day inertia–gravity waves, 4-day MRG waves, or even possibly the largest mesoscale convective systems (Houze 2004; Kiladis et al. 2009; Wang and Liu 2011), could constitute the high-frequency component, whose vertical structure mostly implies damping effects to the MJO circulation except for below 500 hPa.

Figure 9 displays vertical profiles of the regression of decomposed vertical advection terms onto TRMM 3B42 precipitation over the NSA. Again, it is apparent that the low-frequency (black) and high-frequency (red) components account for the largest fraction of total vertical advection, whereas the second and third terms in Eq. (2) are negligible. In addition, the three-layer vertical structure of the high-frequency vertical advection term related to convection is evident in Fig. 9.

Since meridional advection appears to have a discernible damping effect on the MJO circulation (see Fig. 6b), we also further decompose this term in a similar fashion as the vertical advection term. Figure 10 shows time–pressure plots of each decomposed term of meridional advection averaged over the NSA. In contrast to the vertical advection decomposition shown in Fig. 8a where the low-frequency component ($-\overline{\omega}\partial\overline{u}/\partial p$) is dominant for all the MJOs, the low-frequency component ($-\overline{v}\partial\overline{u}/\partial y$; Fig. 10a) for meridional advection is only dominant for the MJO3 active phase in late December. On the contrary, the high-frequency mode ($-v'\partial u'/\partial y$; Fig. 10d) of the meridional advection with two-layer vertical structure has discernable amplitude for the MJO1 and MJO2 active phases. The other terms are quite small. The southward shift of convection for MJO3 (Fig. 1b) and its associated circulation may explain the dominance of the low-frequency component and the weakness of the high-frequency component for the third MJO compared to the earlier two MJO events.

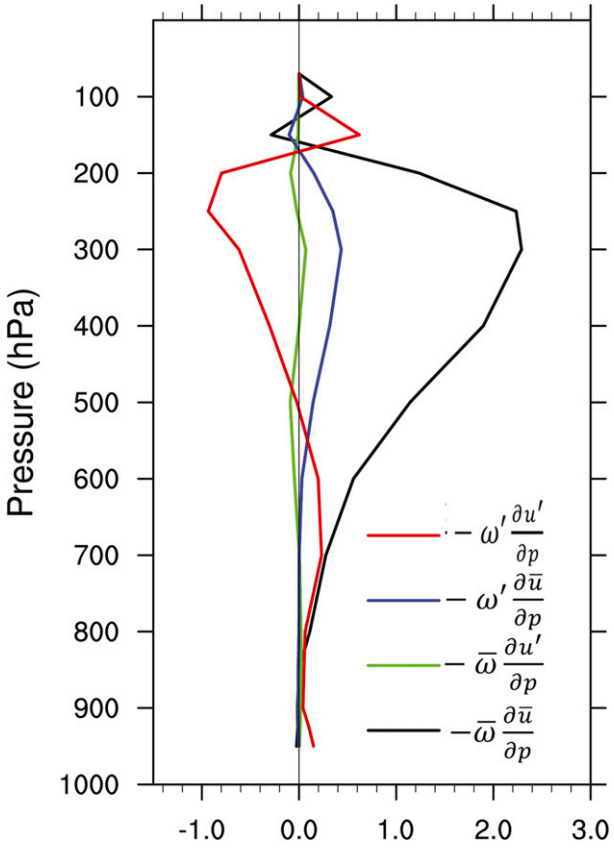

FIG. 9. Profiles of decomposed vertical advection terms ($m\,s^{-1}\,day^{-1}$) regressed onto TRMM rain rate averaged over the NSA from 1 Oct to 31 Dec 2011. Regressed individual terms are averaged over the NSA.

5. Case study: November MJO

Two synoptic-scale WWEs spaced a few days apart during MJO2 in late November are examined in more detail in this section, particularly in light of the relationships among the momentum budget terms we have found in this study thus far regarding the establishment of the zonal-wind structure.

Figure 11a is a time–pressure diagram showing the 6-hourly evolution of the NSA-averaged zonal wind from 21 to 30 November, coincident with the active phase of MJO2 over the IO. Embedded within the prolonged baroclinic structure of zonal wind with the low-level westerlies and easterlies aloft established from 23 November in association with the MJO2, two slantwise WWEs are evident with double maxima at 600 hPa on 25 November and at 700 hPa on 28 November. We refer to the former westerly wind event as WWE1 and the latter event as WWE2. The vertical structure of WWE1 developing from near the surface is more tilted with height and becomes deeper than that of WWE2. Each WWE is preceded by an increase in the magnitude of Q_1 (Fig. 11b) that denotes enhanced convection over the NSA. The tilted vertical structure of the former Q_1 profile is pronounced, which suggests a stepwise evolution of cloud populations documented by Johnson et al. (2015). On the other hand, the latter Q_1 profile is more top heavy than the former one, suggesting the WWE2 is more related to a stratiform rain process (Lin et al. 2004; Xu and Rutledge 2014; Johnson et al. 2015).

Figures 11c–f are as in Figs. 4a–d, but for the MJO2 without 5-day smoothing in order to retain a 6-hourly varying signal. The local time rate of change of the zonal wind denoted by overlaid contours in each panel clearly depicts westerly acceleration (solid contours) preceding the actual occurrence of the WWE. While the westerly acceleration related to WWE1 develops from the surface on 23 November and reaches up to 150 hPa with a tilted vertical structure, the WWE2 westerly acceleration appears on 26 November and deepens only up to 500 hPa. As the local tendency of zonal wind is governed by the Eq. (1), we also display the individual terms from Eq. (1) in Figs. 11c–f except for the Coriolis force and residual terms owing to their smaller magnitude in order to determine which terms in Eq. (1) are primarily responsible for inducing the WWEs during MJO2. Interestingly, notable differences in relative magnitude of individual terms in the momentum budget between WWE1 and WWE2 are detected in Figs. 11c–f. The relationships among the terms associated with WWE1 are consistent with the common features based on all three MJO events that have been discussed—notably a dominant westerly acceleration due to the PGF (Fig. 11f) partly offset by the meridional advection of zonal wind in lower troposphere (Fig. 11d) and westerly acceleration by the vertical advection mostly concentrated in the mid-troposphere (Fig. 11e). In contrast for WWE2, the zonal and meridional advection in the lower troposphere become more in phase with the local tendency of zonal wind than the PGF (Figs. 11c,d,f). Not only is the magnitude of the PGF at lower level remarkably reduced, but also its sign becomes negative at the beginning stage of WWE2. The vertical advection, which is mostly out of phase with the local tendency of zonal wind, shows little, if any, tilt with height and is confined between 500 and 200 hPa.

Figure 12 shows the time series of the PGF, horizontal advection, and local tendency terms averaged between 1000 and 700 hPa over the NSA. The in-phase relationship between the PGF and local tendency is evident from 23 to 25 November, whereas horizontal advection shows a clear out-of-phase relationship with the local tendency. Thus, the westerly acceleration between 1000

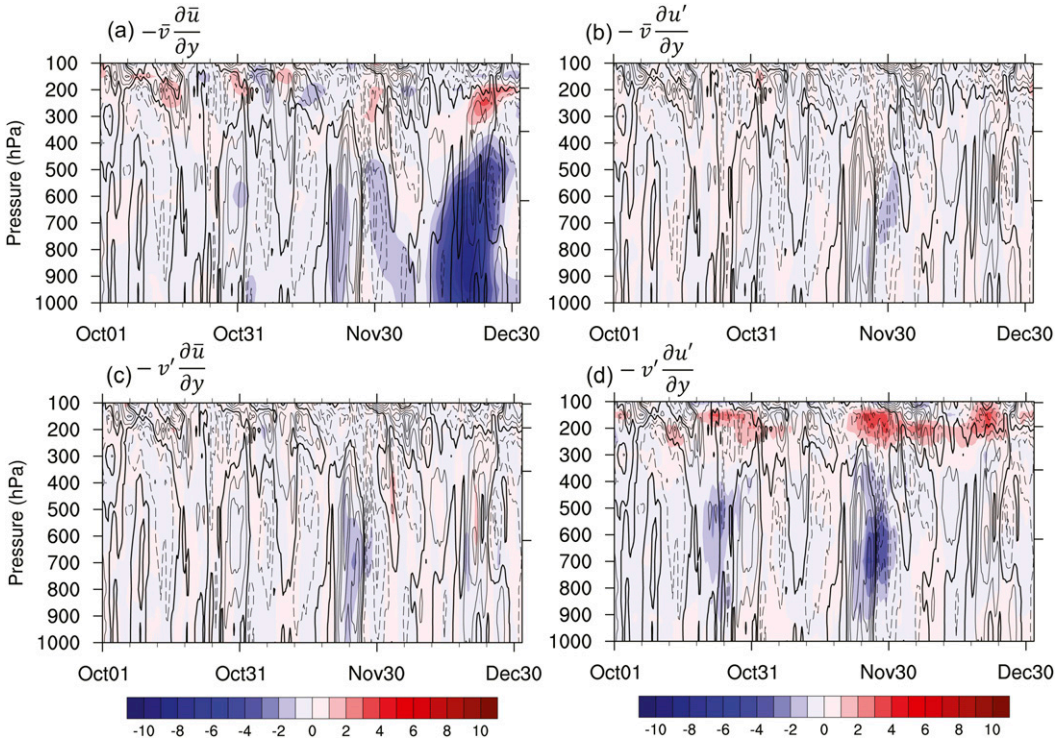

FIG. 10. As in Fig. 8, but for the decomposed meridional advection: (a) $-\bar{v}\partial\bar{u}/\partial y$, (b) $-\bar{v}\partial u'/\partial y$, (c) $-v'\partial\bar{u}/\partial y$, and (d) $-v'\partial u'/\partial y$.

and 700 hPa for WWE1 is most attributable to the PGF. In contrast, the local westerly tendency emerging on 26 November in association with the WWE2 shows a reversed relationship—that is, in phase with the horizontal advection and out of phase with the PGF. This different relationship among the local tendency, PGF, and horizontal advection terms for WWE2 suggests that different dynamic processes are responsible for these WWEs.

To further elucidate why zonal advection plays a critical role for the establishment of WWE2 and its potential contributions from CCWs, the signals of Kelvin, ER, and MRG waves are identified during MJO2 by applying a wavenumber–frequency filter based on Wheeler and Kiladis (1999) but without equatorial symmetry constraints to the zonal wind. Table 1 contains the range of the wavenumbers and periods used for this filtering, and Fig. 13 displays time–pressure diagrams of the identified waves in the zonal wind averaged over the NSA. Since the time axis in Fig. 13 runs from left to right, a rightward (leftward) tilt with height is analogous to a westward (eastward) tilt with height in a pressure–longitude diagram.

As illustrated in Fig. 13a, two Kelvin wave events are evident during MJO2 with patterns of alternating zonal wind displaying westward tilt with height from the surface to around 150 hPa. Westerly phases start on 24 and 27 November from low levels following the increase in Q_1 by 1 day (see Fig. 11b). The vertical structure in zonal wind, which appears like a boomerang, is also seen in Roundy (2008) and three positive maxima near the surface, 500 hPa, and 150 hPa, associated with the former Kelvin wave, are consistent with patterns found by Yang et al. (2007). The westerly phases at lower levels coincide with the timing when the WWEs reach their maxima at 600 and 700 hPa on 25 and 28 November (Fig. 11a), respectively.

On the other hand, the leftward (i.e., eastward)-tilted ER wave identified in the zonal wind (Fig. 13b), with the lowest frequency among three waves presented in Fig. 13, shows deep westerlies throughout the troposphere during the targeted period. This nearly equivalent barotropic vertical structure is also present in Kiladis and Wheeler (1995), in which they relate ER waves to westerly wind bursts.

We also attempt to identify the MRG wave in the zonal wind by using the wavenumber–frequency filter during the MJO2. Figure 13c displays the temporal evolution of vertical structure of the MRG wave in zonal wind during MJO2. With an eastward tilt with height, the MRG wave, having a first-baroclinic-mode structure in the vertical as documented by Yang et al. (2007),

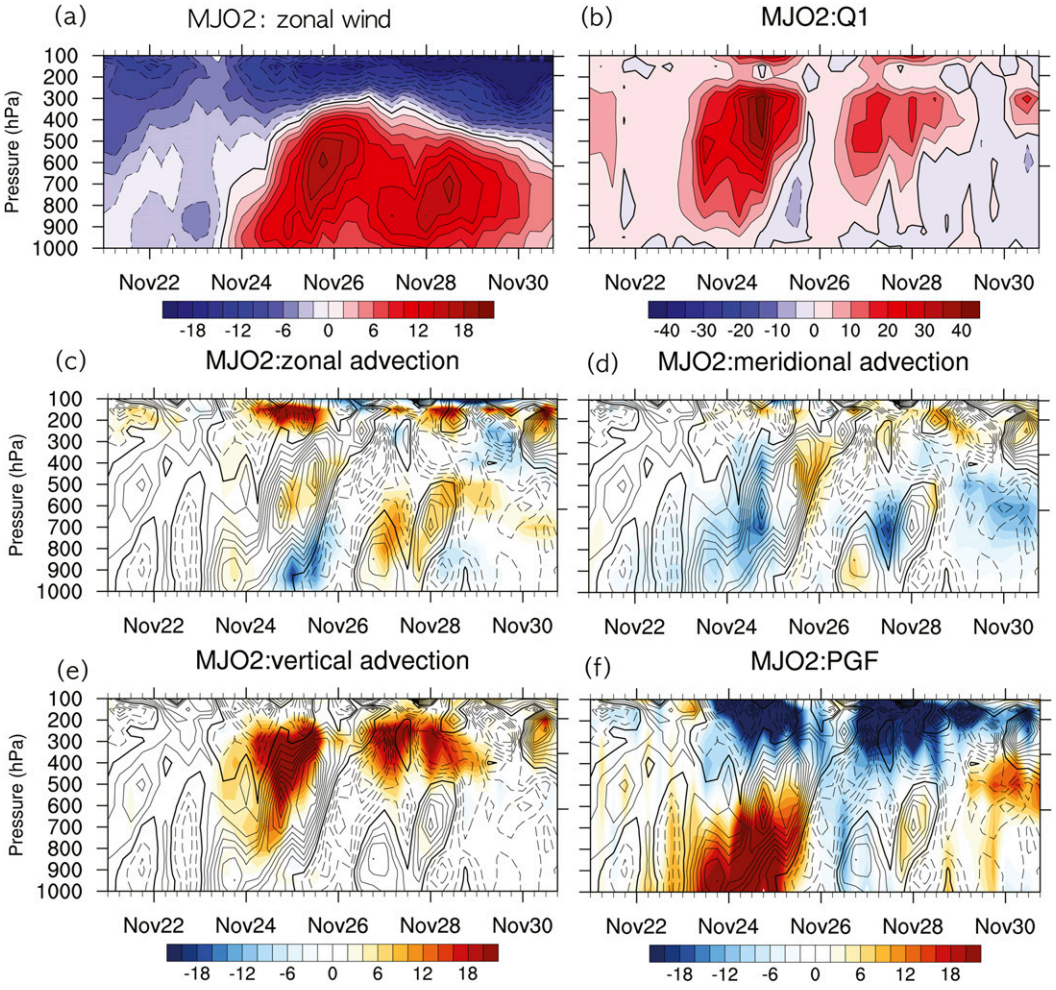

FIG. 11. Time–pressure diagram of NSA-averaged (a) zonal wind ($m\,s^{-1}$), (b) Q_1 ($K\,day^{-1}$), (c) zonal advection, (d) meridional advection, (e) vertical advection, and (f) pressure gradient force. Zonal-wind tendency is overlaid (contours; dashed for negative values; solid for positive values) in (c)–(f). Unit is $m\,s^{-1}\,day^{-1}$ in (c)–(f).

is predominant in association with WWE2 around 27 November. It is coincident with a westward-moving low-level cyclonic circulation identified by Judt and Chen (2014) and Kerns and Chen (2014). They also attributed this synoptic-scale low pressure system to a MRG wave–like system.

In Fig. 14, we further compare low-level-averaged (from 1000 to 700 hPa) values of the zonal wind during MJO2 among the Kelvin, Rossby, and MRG wave components as well as the temporal mean for the entire DYNAMO observing period (October 2011–March 2012) for which the wave filtering is applied. Westerlies associated with the ER wave persist during the entire targeted period with its peak on 25 November exceeding the period mean by $1.7\,m\,s^{-1}$. In addition, two westerly phases related to the Kelvin wave are present on 24–25 and 27–30 November. On the other hand, a westerly component related to the MRG wave becomes apparent in the later stage of MJO2 on 26 November, interestingly coincident with the period when the horizontal advection term becomes in phase with the local wind tendency as shown in Fig. 12. The first maximum of total zonal wind on 25 November (Fig. 11a) is likely linked to the linear superposition of the Rossby and Kelvin wave peaks associated with its first westerly phase induced primarily by strong convection at this time. The second maximum on 28 November can be attributed to the concurrence of all three modes in their westerly phase.

We have noted from Fig. 12 that during WWE2, an in-phase relationship between the local tendency of zonal wind and horizontal advection becomes dominant, whereas the PGF tends to have out-of-phase relationships with the local tendency. Figure 15a

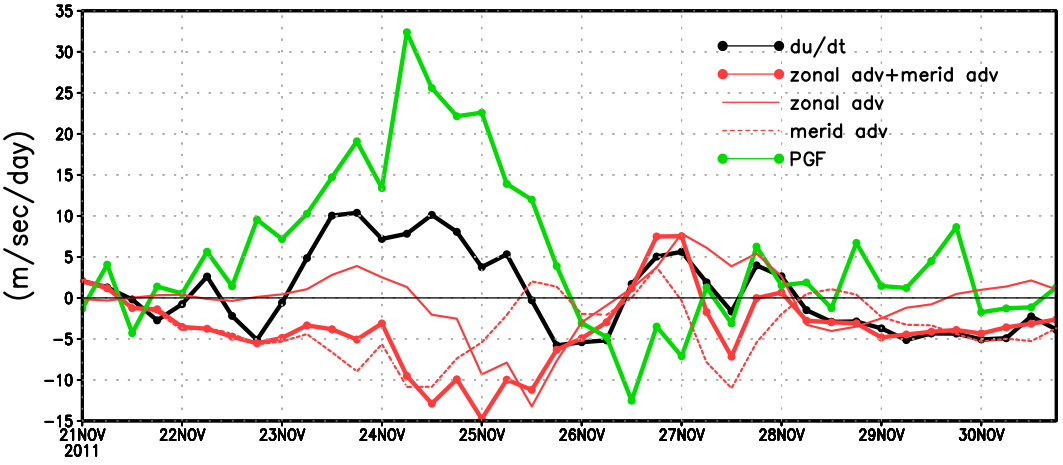

FIG. 12. Time series of individual terms of zonal momentum budget averaged between 1000 and 700 hPa over the NSA.

displays a horizontal map of the zonal advection that accounts for the largest part of low-level westerly acceleration and total wind fields at 850 hPa on 27 November when the low-level-averaged local tendency of zonal wind reaches its second peak in Fig. 12. Collocated with a strong cross-equatorial flow, a southwest–northeast elongated area of strong westerly acceleration due to zonal advection is prominent over the NSA. While westerlies prevail near the equator on the western side of the sounding arrays, two gyres located to the northwest and southeast of the NSA produce confluence over the NSA, resulting in the strong southwesterly flow.

Figures 15b–e show an increasing synthesis of the Kelvin, Rossby, and MRG wave–filtered circulations on 27 November, each with TRMM rain rate (shading) overlaid, and finally with the mean circulation for the entire DYNAMO observing period. It is clearly seen that the NSA is dominated by heavy precipitation during this period. Figure 15b shows only Kelvin wave–filtered circulation (vectors). Westerlies are prevalent to the west of and in the heavy-rainfall region over the NSA, whereas weak easterlies are present in a limited region to the east of NSA. These easterlies could be weakened by the westerlies associated with the previous Kelvin wave event. Figure 15c displays circulations obtained by the superposition of the Kelvin and Rossby wave–filtered winds. A clockwise circulation to the southeast of the NSA as well as a counterclockwise circulation to its northwest emerges along with an increase in westerlies over the NSA. By adding the MRG wave–filtered winds, Fig. 15d illustrates the more expanded and apparent clockwise circulation to the east of the NSA and an even stronger cross-equatorial flow over the NSA. Finally, when the mean circulation (Fig. 14e) is added in, circulations over regions far from the NSA, associated with weaker rainfall, become comparable to the total circulation shown in Fig. 15a.

6. Summary and conclusions

The multinational cooperative DYNAMO field campaign conducted over the Indian Ocean (IO) during late 2011–early 2012 was devoted to advancement in understanding of the MJO dynamics and initiation processes. Three pronounced MJOs, each accompanying one or more WWEs, occurred in late October, late November, and late December 2011. All prominent low-level westerly winds lasting from a few days to 2 weeks associated with the MJO active phases are referred to as WWEs in this study. A zonal momentum budget analysis has been carried out to understand the respective contributions of the dynamical processes involved in the wind evolution associated with the three MJO events over the IO. Our analysis used the ECMWF operational analysis, which has relatively fine spatial resolution (0.25°) and took advantage of the intensive observations during

TABLE 1. Wavenumber and frequency filters for the selected CCEWs. Negative wavenumber indicates westward propagation.

Wave	Wavenumber	Period (days)
Kelvin	1–14	2.5–20
Rossby	−(1–10)	9–72
MRG	−(1–10)	3–10

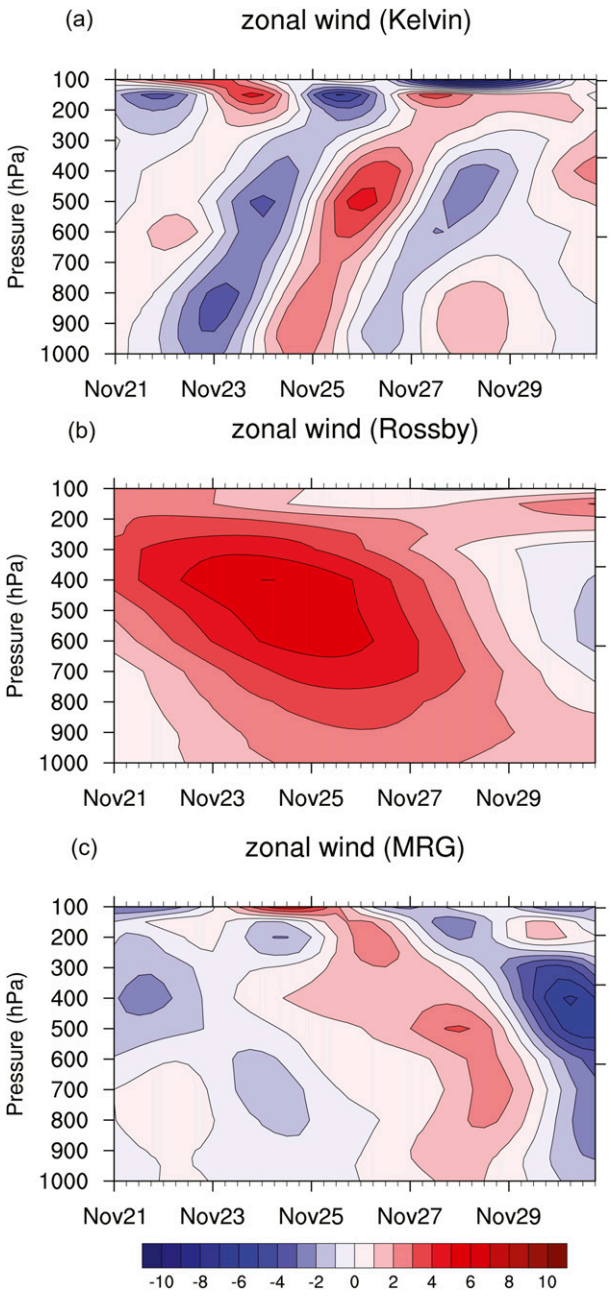

FIG. 13. Time–pressure diagram of (a) Kelvin, (b) Rossby, and (c) MRG wave–filtered zonal wind (m s^{-1}) averaged over the NSA during MJO2.

DYNAMO. We focused our analyses over the Northern Sounding Array (NSA) of DYNAMO when the MJO signal was strongest during the October–December 2011 period.

As a result, we have found that the westerly (easterly) acceleration at lower (upper) levels induced by the pressure gradient force (PGF) accounts for the establishment of a baroclinic wind structure over the NSA following MJO convection. Along with the PGF, vertical advection that is closely linked to convection transports westerly momentum upward, resulting in a westerly acceleration in the midtroposphere. By further decomposing the zonal-wind and pressure velocity fields that make up the vertical advection term into low-frequency (5-day running mean) and high-frequency (deviation from 5-day running mean) components, the relative contribution of these components to the total vertical advection associated with MJO active phase is examined. While the low-frequency component accounts for a considerable fraction of the total vertical advection, the high-frequency component exhibits an intriguing three-layer vertical structure with positive signs in the upper and lower troposphere and a negative sign in the midtroposphere. This structure resembles the findings by Mechem et al. (2006) and Miyakawa et al. (2012) based on cloud-resolving models and by Oh et al. (2015) based on reanalysis data.

In contrast, the meridional (zonal) advection at lower (upper) level cancels the westerly (easterly) acceleration effect by the PGF, damping the MJO circulation. Inconsistent with previous studies emphasizing a possible role of the budget residual in the westerly acceleration in the lower level, the residual in our study based on the ECMWF analysis with much finer spatial resolution only damps the preexisting easterly flow in the very upper troposphere, possibly as a result of detrainment near the cloud top. We speculate that this inconsistency could be attributable to the difference in the spatial resolution of datasets. With higher resolution, more of the convective transports are resolved, thus reducing the residual, as Arakawa (2004) pointed out for the moist static energy budget.

Our momentum budget analysis of westerly wind events associated with the MJO identified some competing mechanisms that stem from the dynamics of organized precipitating convection. The rearward vertical tilt of mesoscale convective systems relative to the environmental shear vector, referred to as slantwise layer overturning by Moncrieff (2004), can increase the vertical shear and transfer kinetic energy upscale to the large-scale flow. This competes with the dissipative nature of turbulent cumulus convection. The work done by the horizontal pressure gradient normalized by the kinetic energy available from shear and propagation is a key aspect (Moncrieff 1992). The rearward tilt of mesoscale convective systems relative to their direction of propagation affects the sign of the momentum transport; for example, eastward-propagating mesoscale systems generate westward momentum transport. Therefore, the zonal momentum tendency (the negative of the vertical gradient of momentum transport) in the lower

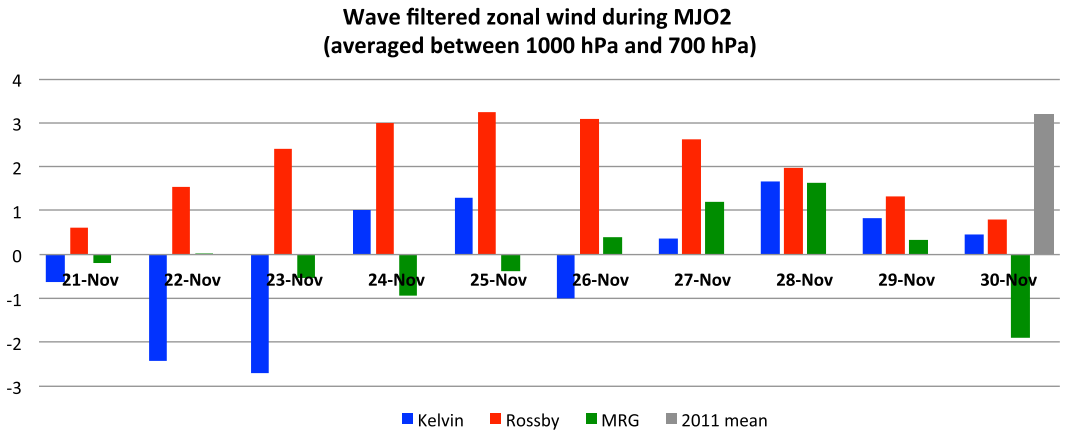

FIG. 14. Lower-level (from 1000 to 700 hPa) average of Kelvin, Rossby, and MRG wave–filtered zonal wind along with temporal mean of DYNAMO observing period (1 Oct 2011–31 Mar 2012) averaged over the NSA for MJO2 ($m\,s^{-1}$).

troposphere accelerates the westerly wind. The above effects of organized mesoscale systems also apply to synoptic-scale superclusters. Moncrieff and Klinker (1997) identified another competing mechanism: organized convective momentum transport has the opposite sign from the parameterized subgrid momentum transport. Finally, the reason why the meridional transport of zonal momentum shown in our analysis acts to decrease the westerly wind may be due to tilted Rossby gyres. More complete descriptions of the above dynamical mechanisms are published in Moncrieff (2010). It is likely that the effects of the above competing mechanisms are resolution dependent—an aspect that certainly warrants further investigation.

Two WWEs spaced a few days apart during the active phase of MJO2 in late November are further examined on the basis of a 6-hourly evolving momentum budget analysis. The in-phase relationship between the PGF and local tendency in the lower level is pronounced in terms of the first WWE, whereas horizontal advection shows a clear out-of-phase relationship with the local tendency. However, interestingly, the local positive u tendency associated with the second WWE shows a reverse relationship (i.e., in phase with the horizontal advection, out of phase with the PGF). The different relationships among the local tendency, PGF, and horizontal advection in terms of WWEs during MJO2 suggest that different dynamic processes are impacting the occurrence of WWEs.

To explore this possibility, the dynamical contributions of synoptic-scale CCWs to the WWEs during MJO2 are also considered by isolating the signals of Kelvin, equatorial Rossby, and MRG waves from the zonal wind. The first zonal-wind maximum associated with the former WWE is likely due to the superposition of the Rossby and Kelvin wave–filtered westerly peaks, whereas the second maximum associated with the latter WWE can be attributed to the coherence of the Kelvin, ER, and MRG waves in their westerly phase. It is suggested that the emergence of the MRG wave in the MJO2 envelope, especially for the period of latter WWE, is attributable to the in-phase relationship between the low-level horizontal advection and local tendency of zonal wind, distinguishing the two WWEs.

Our results from the momentum budget analyses focusing on three MJO events during DYNAMO are an attempt to derive the common dynamical mechanisms behind WWEs that could lead one to distinguish different intrinsic features among individual WWEs associated with the MJOs. Through a detailed case study, we found that differences in the developing processes among WWEs can be attributed to different types of CCWs. However, in a future study, it would be worthwhile to develop an extended analysis of multiple MJO events using reanalysis data with a longer record and fine spatial resolution to gain generality in these results. In addition, the residual term known to contain the effects of CMT on the zonal-wind tendency deserves detailed investigation by comparisons to the parameterized convective momentum transport in GCMs.

Acknowledgments. We thank Drs. Chidong Zhang and Steve Williams for help with the ECWMF DYNAMO operational analysis dataset. This work has greatly benefited from stimulating discussions with Dr. D. Kim. We acknowledge support by the NSF Climate and Large-Scale Dynamics Program under Awards AGS-1228302, AGS-1221013, and AGS-1360237 and NOAA

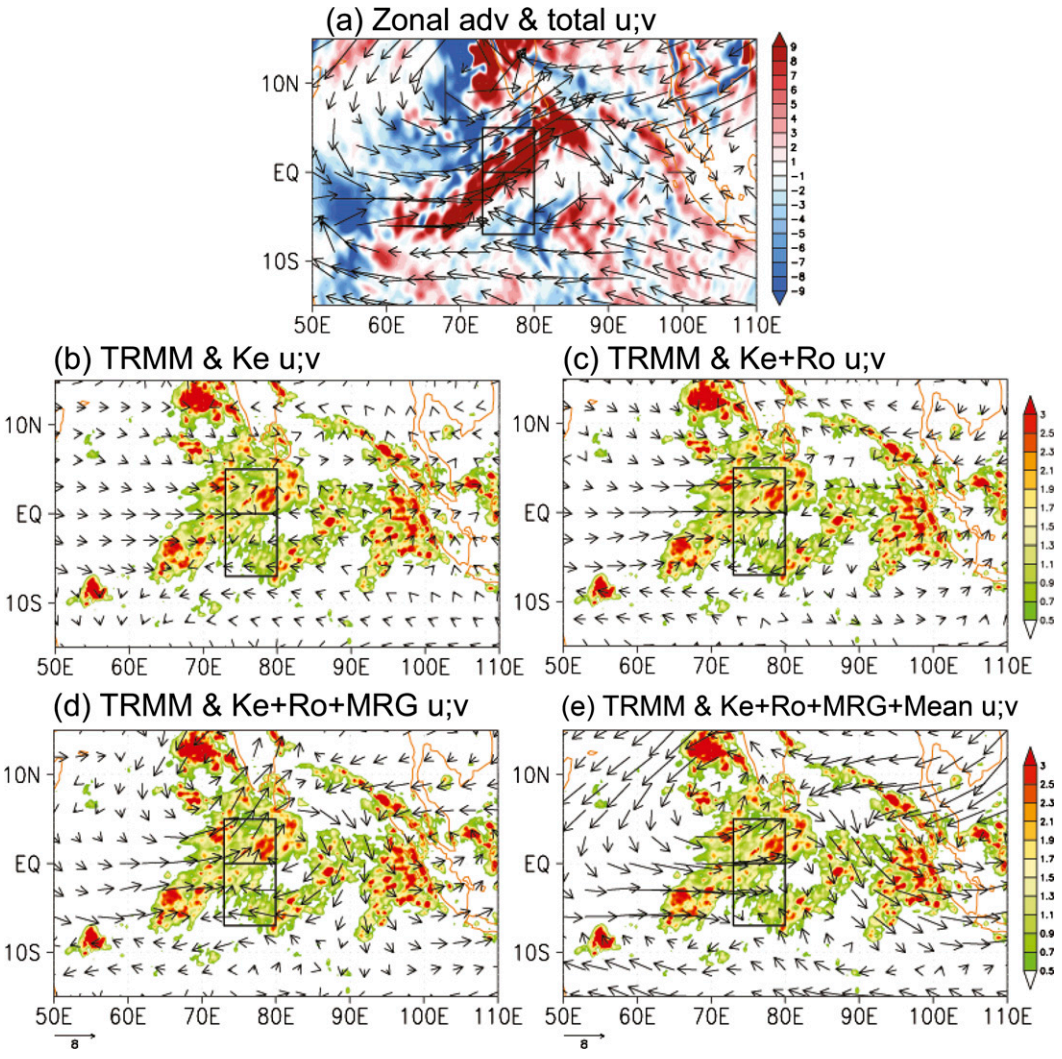

FIG. 15. Snapshot on 27 Nov 2011 at 850 hPa: (a) zonal advection (m s^{-1} day^{-1}; shading) with total winds (m s^{-1}; vectors). (b) Kelvin wave–filtered winds; (c) summation of Kelvin and Rossby wave–filtered winds; (d) summation of Kelvin, Rossby, and MRG wave–filtered winds; and (e) summation of Kelvin, Rossby, and MRG wave–filtered winds and DYNAMO mean winds. Rectangles denote boundaries of the NSA and SSA. TRMM rain rate (mm h^{-1}; shading) is overlaid in (b)–(e).

MAPP Program under Award NA12OAR4310075. Part of this research was carried out at the Jet Propulsion Laboratory, California Institute of Technology, under a contract with the National Aeronautics and Space Administration.

REFERENCES

Arakawa, A., 2004: The cumulus parameterization problem: Past, present, and future. *J. Climate*, **17**, 2493–2525, doi:10.1175/1520-0442(2004)017<2493:RATCPP>2.0.CO;2.

Araligidad, N. M., and E. D. Maloney, 2008: Wind-driven latent heat flux and the intraseasonal oscillation. *Geophys. Res. Lett.*, **35**, L04815, doi:10.1029/2007GL032746.

Barnes, H. C., and R. A. Houze Jr., 2013: The precipitating cloud population of the Madden-Julian Oscillation over the Indian and west Pacific Oceans. *J. Geophys. Res. Atmos.*, **118**, 6996–7023, doi:10.1002/jgrd.50375.

Carr, M. T., and C. S. Bretherton, 2001: Convective momentum transport over the tropical Pacific: Budget estimates. *J. Atmos. Sci.*, **58**, 1673–1693, doi:10.1175/1520-0469(2001)058<1673:CMTOTT>2.0.CO;2.

Chiodi, A. M., D. E. Harrison, and G. A. Vecchi, 2014: Subseasonal atmospheric variability and El Niño waveguide warming: Observed effects of the Madden–Julian oscillation and westerly wind events. *J. Climate*, **27**, 3619–3642, doi:10.1175/JCLI-D-13-00547.1.

Ciesielski, P. E., and Coauthors, 2014: Quality-controlled upper-air sounding dataset for DYNAMO/CINDY/AMIE: Development and corrections. *J. Atmos. Oceanic Technol.*, **31**, 741–764, doi:10.1175/JTECH-D-13-00165.1.

DePasquale, A., C. Schumacher, and A. Rapp, 2014: Radar observations of MJO and Kelvin wave interactions during

DYNAMO/CINDY2011/AMIE. *J. Geophys. Res. Atmos.*, **119**, 6347–6367, doi:10.1002/2013JD021031.

Fu, X., J.-Y. Lee, P.-C. Hsu, H. Taniguchi, B. Wang, W. Wang, and S. Weaver, 2013: Multi-model MJO forecasting during DYNAMO/CINDY period. *Climate Dyn.*, **41**, 1067–1081, doi:10.1007/s00382-013-1859-9.

Gottschalck, J., P. E. Roundy, C. J. Schreck III, A. Vintzileos, and C. Zhang, 2013: Large-scale atmospheric and oceanic conditions during the 2011–12 DYNAMO field campaign. *Mon. Wea. Rev.*, **141**, 4173–4196, doi:10.1175/MWR-D-13-00022.1.

Gregory, D., 1997: Parametrization of convective momentum transports in the ECMWF model: Evaluation using cloud resolving models and impact upon model climate. *Proc. ECMWF Workshop on New Insights and Approaches to Convective Parametrization*, Reading, United Kingdom, ECMWF, 208–227.

Hendon, H. H., M. C. Wheeler, and C. Zhang, 2007: Seasonal dependence of the MJO–ENSO relationship. *J. Climate*, **20**, 531–543, doi:10.1175/JCLI4003.1.

Houze, R. A., Jr., 2004: Mesoscale convective systems. *Rev. Geophys.*, **42**, RG4003, doi:10.1029/2004RG000150.

——, S. S. Chen, D. E. Kingsmill, Y. Serra, and S. E. Yuter, 2000: Convection over the Pacific warm pool in relation to the atmospheric Kelvin-Rossby wave. *J. Atmos. Sci.*, **57**, 3058–3089, doi:10.1175/1520-0469(2000)057<3058:COTPWP>2.0.CO;2.

Huffman, G. J., R. F. Adler, B. Rudolf, U. Schneider, and P. R. Keehn, 1995: Global precipitation estimates based on a technique for combining satellite-based estimates, rain gauge analysis, and NWP model precipitation information. *J. Climate*, **8**, 1284–1295, doi:10.1175/1520-0442(1995)008<1284:GPEBOA>2.0.CO;2.

Jiang, X., D. E. Waliser, J.-L. Li, and C. Woods, 2011: Vertical cloud structures of the boreal summer intraseasonal variability based on CloudSat observations and ERA-interim reanalysis. *Climate Dyn.*, **36**, 2219–2232, doi:10.1007/s00382-010-0853-8.

Johnson, R. H., and P. E. Ciesielski, 2013: Structure and properties of Madden–Julian oscillations deduced from DYNAMO sounding arrays. *J. Atmos. Sci.*, **70**, 3157–3179, doi:10.1175/JAS-D-13-065.1.

——, ——, J. H. Ruppert Jr., and M. Katsumata, 2015: Sounding-based thermodynamic budgets for DYNAMO. *J. Atmos. Sci.*, **72**, 598–622, doi:10.1175/JAS-D-14-0202.1.

Judt, F., and S. S. Chen, 2014: An explosive convective cloud system and its environmental conditions in MJO initiation observed during DYNAMO. *J. Geophys. Res. Atmos.*, **119**, 2781–2795, doi:10.1002/2013JD021048.

Kerns, B. W., and S. S. Chen, 2014: Equatorial dry air intrusion and related synoptic variability in MJO initiation during DYNAMO. *Mon. Wea. Rev.*, **142**, 1326–1343, doi:10.1175/MWR-D-13-00159.1.

Kessler, W. S., M. J. McPhaden, and K. M. Weickmann, 1995: Forcing of intraseasonal Kelvin waves in the equatorial Pacific. *J. Geophys. Res.*, **100**, 10 613–10 631, doi:10.1029/95JC00382.

Khouider, B., Y. Han, A. J. Majda, and S. N. Stechmann, 2012: Multiscale waves in an MJO background and convective momentum transport feedback. *J. Atmos. Sci.*, **69**, 915–933, doi:10.1175/JAS-D-11-0152.1.

Kiladis, G. N., and M. Wheeler, 1995: Horizontal and vertical structure of observed tropospheric equatorial Rossby waves. *J. Geophys. Res.*, **100**, 22 981–22 997, doi:10.1029/95JD02415.

——, M. C. Wheeler, P. T. Haertel, K. H. Straub, and P. E. Roundy, 2009: Convectively coupled equatorial waves. *Rev. Geophys.*, **47**, RG2003, doi:10.1029/2008RG000266.

——, J. Dias, K. H. Straub, M. C. Wheeler, S. N. Tulich, K. Kikuchi, K. M. Weickmann, and M. J. Ventrice, 2014: A comparison of OLR and circulation-based indices for tracking the MJO. *Mon. Wea. Rev.*, **142**, 1697–1715, doi:10.1175/MWR-D-13-00301.1.

Knutson, T. R., and K. M. Weickmann, 1987: 30–60 day atmospheric oscillations: Composite life cycles of convection and circulation anomalies. *Mon. Wea. Rev.*, **115**, 1407–1436, doi:10.1175/1520-0493(1987)115<1407:DAOCLC>2.0.CO;2.

Lafore, J.-P., and M. W. Moncrieff, 1989: A numerical investigation of the organization and interaction of the convective and stratiform regions of tropical squall lines. *J. Atmos. Sci.,* **46**, 521–544, doi:10.1175/1520-0469(1989)046<0521:ANIOTO>2.0.CO;2.

Lau, W. K., and D. E. Waliser, 2012: *Intraseasonal Variability in the Atmosphere-Ocean Climate System.* 2nd ed. Springer, 614 pp.

Lin, J., B. Mapes, M. Zhang, and M. Newman, 2004: Stratiform precipitation, vertical heating profiles, and the Madden–Julian oscillation. *J. Atmos. Sci.*, **61**, 296–309, doi:10.1175/1520-0469(2004)061<0296:SPVHPA>2.0.CO;2.

——, M. Zhang, and B. Mapes, 2005: Zonal momentum budget of the Madden–Julian oscillation: The source and strength of equivalent linear damping. *J. Atmos. Sci.*, **62**, 2172–2188, doi:10.1175/JAS3471.1.

Lin, X., and R. H. Johnson, 1996: Kinematic and thermodynamic characteristics of the flow over the western Pacific warm pool during TOGA COARE. *J. Atmos. Sci.*, **53**, 695–715, doi:10.1175/1520-0469(1996)053<0695:KATCOT>2.0.CO;2.

Ling, J., P. Bauer, P. Bechtold, A. Beljaars, R. Forbes, F. Vitart, M. Ulate, and C. Zhang, 2014: Global versus local MJO forecast skill of the ECMWF model during DYNAMO. *Mon. Wea. Rev.*, **142**, 2228–2247, doi:10.1175/MWR-D-13-00292.1.

Madden, R. A., and P. R. Julian, 1971: Detection of a 40–50 day oscillation in the zonal wind in the tropical Pacific. *J. Atmos. Sci.*, **28**, 702–708, doi:10.1175/1520-0469(1971)028<0702:DOADOI>2.0.CO;2.

——, and ——, 1972: Description of global-scale circulation cells in the tropics with a 40–50 day period. *J. Atmos. Sci.*, **29**, 1109–1123, doi:10.1175/1520-0469(1972)029<1109:DOGSCC>2.0.CO;2.

Maloney, E. D., and A. H. Sobel, 2004: Surface fluxes and ocean coupling in the tropical intraseasonal oscillation. *J. Climate*, **17**, 4368–4386, doi:10.1175/JCLI-3212.1.

Mapes, B., S. Tulich, J. Lin, and P. Zuidema, 2006: The mesoscale convection life cycle: Building block or prototype for large-scale tropical waves? *Dyn. Atmos. Oceans*, **42**, 3–29, doi:10.1016/j.dynatmoce.2006.03.003.

Matthews, A. J., 2008: Primary and successive events in the Madden–Julian oscillation. *Quart. J. Roy. Meteor. Soc.*, **134**, 439–453, doi:10.1002/qj.224.

McPhaden, M. J., S. E. Zebiak, and M. H. Glantz, 2006: ENSO as an integrating concept in earth science. *Science*, **314**, 1740–1745, doi:10.1126/science.1132588.

Mechem, D. B., S. S. Chen, and R. A. Houze, 2006: Momentum transport processes in the stratiform regions of mesoscale convective systems over the western Pacific warm pool. *Quart. J. Roy. Meteor. Soc.*, **132**, 709–736, doi:10.1256/qj.04.141.

Miyakawa, T., Y. N. Takayabu, T. Nasuno, H. Miura, M. Satoh, and M. W. Moncrieff, 2012: Convective momentum transport by rainbands within a Madden–Julian oscillation in a global nonhydrostatic model with explicit deep convective processes. Part I: Methodology and general results. *J. Atmos. Sci.*, **69**, 1317–1338, doi:10.1175/JAS-D-11-024.1.

Moncrieff, M. W., 1992: Organized convective systems: Archetypal models, mass and momentum flux theory, and parameterization. *Quart. J. Roy. Meteor. Soc.*, **118**, 819–850, doi:10.1002/qj.49711850703.

——, 2004: Analytic representation of the large-scale organization of tropical convection. *J. Atmos. Sci.*, **61**, 1521–1538, doi:10.1175/1520-0469(2004)061<1521:AROTLO>2.0.CO;2.

——, 2010: The multiscale organization of moist convection and the intersection of weather and climate. *Climate Dynamics: Why Does Climate Vary? Geophys. Monogr.*, Vol. 189, Amer. Geophys. Union, 3–26, doi:10.1029/2008GM000838.

——, and E. Klinker, 1997: Organized convective systems in the tropical western Pacific as a process in general circulation models. *Quart. J. Roy. Meteor. Soc.*, **123**, 805–828, doi:10.1002/qj.49712354002.

——, D. E. Waliser, M. J. Miller, M. A. Shapiro, G. R. Asrar, and J. Caughey, 2012: Multiscale convective organization and the YOTC virtual global field campaign. *Bull. Amer. Meteor. Soc.*, **93**, 1171–1187, doi:10.1175/BAMS-D-11-00233.1.

Moum, J. N., and Coauthors, 2014: Air–sea interactions from westerly wind bursts during the November 2011 MJO in the Indian Ocean. *Bull. Amer. Meteor. Soc.*, **95**, 1185–1199, doi:10.1175/BAMS-D-12-00225.1.

Nakazawa, T., 1988: Tropical super clusters within intraseasonal variations over the western Pacific. *J. Meteor. Soc. Japan*, **66**, 823–839.

Oh, J.-H., X. Jiang, D. E. Waliser, M. W. Moncrieff, and R. H. Johnson, 2015: Convective momentum transport associated with the Madden–Julian oscillation based on a reanalysis dataset. *J. Climate*, **28**, 5763–5782, doi:10.1175/JCLI-D-14-00570.1.

Roundy, P. E., 2008: Analysis of convectively coupled Kelvin waves in the Indian Ocean MJO. *J. Atmos. Sci.*, **65**, 1342–1359, doi:10.1175/2007JAS2345.1.

Rui, H., and B. Wang, 1990: Development characteristics and dynamic structure of tropical intraseasonal convection anomalies. *J. Atmos. Sci.*, **47**, 357–379, doi:10.1175/1520-0469(1990)047<0357:DCADSO>2.0.CO;2.

Seiki, A., and Y. N. Takayabu, 2007: Westerly wind bursts and their relationship with intraseasonal variations and ENSO. Part I: Statistics. *Mon. Wea. Rev.*, **135**, 3325–3345, doi:10.1175/MWR3477.1.

——, ——, T. Yasuda, N. Sato, C. Takahashi, K. Yoneyama, and R. Shirooka, 2011: Westerly wind bursts and their relationship with ENSO in CMIP3 models. *J. Geophys. Res.*, **116**, D03303, doi:10.1029/2010JD015039.

Sobel, A. H., E. D. Maloney, G. Bellon, and D. M. Frierson, 2008: The role of surface heat fluxes in tropical intraseasonal oscillations. *Nat. Geosci.*, **1**, 653–657, doi:10.1038/ngeo312.

——, ——, ——, and ——, 2010: Surface fluxes and tropical intraseasonal variability: A reassessment. *J. Adv. Model. Earth Syst.*, **2**, 2, doi:10.3894/JAMES.2010.2.2.

——, S. Wang, and D. Kim, 2014: Moist static energy budget of the MJO during DYNAMO. *J. Atmos. Sci.*, **71**, 4276–4291, doi:10.1175/JAS-D-14-0052.1.

Straub, K. H., 2013: MJO initiation in the real-time multivariate MJO index. *J. Climate*, **26**, 1130–1151, doi:10.1175/JCLI-D-12-00074.1.

Takayabu, Y. N., 1994: Large-scale cloud disturbances associated with equatorial waves. Part II: Westward-propagating inertio-gravity waves. *J. Meteor. Soc. Japan*, **72**, 451–465.

——, T. Iguchi, M. Kachi, A. Shibata, and H. Kanzawa, 1999: Abrupt termination of the 1997–98 El Niño in response to a Madden–Julian oscillation. *Nature*, **402**, 279–282, doi:10.1038/46254.

Trier, S. B., M. A. LeMone, and W. C. Skamarock, 1998: Effect of three-dimensional structure on the stormwide horizontal accelerations and momentum budget of a simulated squall line. *Mon. Wea. Rev.*, **126**, 2580–2598, doi:10.1175/1520-0493(1998)126<2580:EOTDSO>2.0.CO;2.

Tung, W.-W., and M. Yanai, 2002a: Convective momentum transport observed during the TOGA COARE IOP. Part I: General features. *J. Atmos. Sci.*, **59**, 1857–1871, doi:10.1175/1520-0469(2002)059<1857:CMTODT>2.0.CO;2.

——, and ——, 2002b: Convective momentum transport observed during the TOGA COARE IOP. Part II: Case studies. *J. Atmos. Sci.*, **59**, 2535–2549, doi:10.1175/1520-0469(2002)059<2535:CMTODT>2.0.CO;2.

Wang, B., and F. Liu, 2011: A model for scale interaction in the Madden–Julian oscillation. *J. Atmos. Sci.*, **68**, 2524–2536, doi:10.1175/2011JAS3660.1.

Wang, S., A. H. Sobel, F. Zhang, Y. Q. Sun, Y. Yue, and L. Zhou, 2015: Regional simulation of the October and November MJO events observed during the CINDY/DYNAMO field campaign at gray zone resolution. *J. Climate*, **28**, 2097–2119, doi:10.1175/JCLI-D-14-00294.1.

Wheeler, M., and G. N. Kiladis, 1999: Convectively coupled equatorial waves: Analysis of clouds and temperature in the wavenumber–frequency domain. *J. Atmos. Sci.*, **56**, 374–399, doi:10.1175/1520-0469(1999)056<0374:CCEWAO>2.0.CO;2.

——, and H. H. Hendon, 2004: An all-season real-time multivariate MJO index: Development of an index for monitoring and prediction. *Mon. Wea. Rev.*, **132**, 1917–1932, doi:10.1175/1520-0493(2004)132<1917:AARMMI>2.0.CO;2.

Xu, W., and S. A. Rutledge, 2014: Convective characteristics of the Madden–Julian oscillation over the central Indian Ocean observed by shipborne radar during DYNAMO. *J. Atmos. Sci.*, **71**, 2859–2877, doi:10.1175/JAS-D-13-0372.1.

Yanai, M., B. Chen, and W.-W. Tung, 2000: The Madden–Julian oscillation observed during the TOGA COARE IOP: Global view. *J. Atmos. Sci.*, **57**, 2374–2396, doi:10.1175/1520-0469(2000)057<2374:TMJOOD>2.0.CO;2.

Yang, G.-Y., B. Hoskins, and J. Slingo, 2007: Convectively coupled equatorial waves. Part I: Horizontal and vertical structures. *J. Atmos. Sci.*, **64**, 3406–3423, doi:10.1175/JAS4017.1.

Yang, M.-J., and R. A. Houze Jr., 1996: Momentum budget of a squall line with trailing stratiform precipitation: Calculations with a high-resolution numerical model. *J. Atmos. Sci.,* **53**, 3629–3652, doi:10.1175/1520-0469(1996)053<3629:MBOASL>2.0.CO;2.

Yoneyama, K., C. Zhang, and C. N. Long, 2013: Tracking pulses of the Madden–Julian oscillation. *Bull. Amer. Meteor. Soc.*, **94**, 1871–1891, doi:10.1175/BAMS-D-12-00157.1.

Zhang, C., 2005: Madden-Julian Oscillation. *Rev. Geophys.*, **43**, RG2003, doi:10.1029/2004RG000158.

——, J. Gottschalck, E. D. Maloney, M. W. Moncrieff, F. Vitart, D. E. Waliser, B. Wang, and M. C. Wheeler, 2013: Cracking the MJO nut. *Geophys. Res. Lett.*, **40**, 1223–1230, doi:10.1002/grl.50244.

Zuluaga, M. D., and R. A. J. Houze, 2013: Evolution of the population of precipitating convective systems over the equatorial Indian Ocean in active phases of the Madden–Julian Oscillation. *J. Atmos. Sci.*, **70**, 2713–2725, doi:10.1175/JAS-D-12-0311.1.